ICES REPORT 12-23

June 2012

Isogeometric boundary element analysis using unstructured T-splines

by

M. A. Scott, R. N. Simpson, J. A. Evans, S. Lipton, S. P. A. Bordas, T. J. R. Hughes, T. W. Sederberg

The Institute for Computational Engineering and Sciences
The University of Texas at Austin
Austin, Texas 78712

Reference: M. A. Scott, R. N. Simpson, J. A. Evans, S. Lipton, S. P. A. Bordas, T. J. R. Hughes, T. W. Sederberg, Isogeometric boundary element analysis using unstructured T-splines, ICES REPORT 12-23, The Institute for Computational Engineering and Sciences, The University of Texas at Austin, June 2012.

Isogeometric boundary element analysis using unstructured T-splines

M. A. Scott[d,*], R. N. Simpson[b], J. A. Evans[a], S. Lipton[a], S. P. A. Bordas[b], T. J. R. Hughes[a], T. W. Sederberg[c]

[a] *Institute for Computational Engineering and Sciences, The University of Texas at Austin, Austin, Texas 78712, USA*
[b] *Institute of Mechanics and Advanced Materials, School of Engineering, Cardiff University, Queen's Buildings, The Parade, Cardiff CF24 3AA, Wales,UK*
[c] *Department of Computer Science, Brigham Young University, Provo, Utah 84602, USA*
[d] *Department of Civil and Environmental Engineering, Brigham Young University, Provo, Utah 84602, USA*

Abstract

We couple collocated isogeometric boundary element methods and unstructured analysis-suitable T-spline surfaces for linear elastostatic problems. We extend the definition of analysis-suitable T-splines to encompass unstructured control grids (unstructured meshes) and develop basis functions which are smooth (rational) polynomials defined in terms of the Bézier extraction framework and which pass standard patch tests. We then develop a collocation procedure which correctly accounts for sharp edges and corners, extraordinary points, and T-junctions. This approach is applied to several three-dimensional problems, including a real-world T-spline model of a propeller. We believe this work clearly illustrates the power of combining new analysis-suitable computer aided design technologies with established analysis methodologies, in this case, the boundary element method.

Keywords: isogeometric analysis, T-splines, boundary elements, design-through-analysis, collocation

1. Introduction

There is an increasing demand for tighter integration and sophistication of the tools and technologies which underlie modern design-through-analysis frameworks. This trend is fueled by the promise of reduced costs and turn-around times in the engineering product lifecycle and the demand for higher fidelity and complexity in modern engineered systems. Fundamental to the accomplishment of this objective is the development of technology which unifies and improves upon the basic components of each subsystem. In this spirit, we couple isogeometric boundary element methods

*Corresponding author
Email address: michael.scott@byu.edu (M. A. Scott)

and T-spline surfaces of arbitrary topology. This approach entirely eliminates geometry clean-up and feature removal steps, and traditional mesh generation. Indeed, the T-spline design is also the analysis model. This approach can be applied directly to engineering surface designs of arbitrary complexity, automatically, at any point during the design-through-analysis iterative cycle. The geometrically exact and smooth T-spline combined with the boundary element method is demonstrated on several benchmark problems. Additionally, a T-spline propeller model is analyzed to demonstrate the feasibility of the method on real-world engineering designs. We focus on linear elasticity in this paper but note that the approach is general and can be applied to any suitable boundary element formulation.

1.1. Isogeometric analysis

Isogeometric Analysis (IGA) has emerged as an important alternative to traditional design and analysis methodologies. IGA, introduced in the Finite Element Analysis (FEA) community [1, 2], establishes a fundamental link with Computer Aided Design (CAD) geometry by using the geometric basis directly as the basis for analysis. Consequently, the finite element mesh *is* an exact representation of the geometry.

A surprising development in the initial NURBS-based isogeometric investigations was the tremendous computational advantages that smoothness offers over standard finite elements [3, 4]. Areas of application of NURBS-based isogeometric analysis are varied and continue to grow rapidly. A small sampling includes fluids and turbulence [5, 6, 7, 8], fluid-structure interaction [9, 10, 11, 12], incompressibility [13, 14, 15], structural and vibration analysis [16, 3], plates and shells [17, 18, 19, 20, 21], phase-field analysis [22, 23, 24], large deformation structural analysis with severe mesh distortion [25], shape optimization [26, 27, 28, 29], and electromagnetics [30]. Interestingly, this success has attracted researchers within the Computer Aided Geometric Design (CAGD) community to develop new "analysis-aware" geometric technologies [31, 32, 33, 34, 35, 36, 37, 38].

1.2. T-splines

While isogeometric analysis represents an important step forward there still remains basic limitations in the predominantly NURBS-based engineering design approaches of today. NURBS are severely limited by the simple fact that they are four sided. In traditional NURBS-based design, modeling a complicated engineering design often requires hundreds, if not thousands, of NURBS patches which are usually discontinuous across patch boundaries. As an example, a multi-patch NURBS representation of the single T-spline in Figure 21 is shown in Figure 23. In this case, 72 NURBS patches are required to construct the same geometry. The complexity of the patch layout coupled with the manual enforcement of smoothness across patch boundaries (via control point positioning) makes NURBS design of complicated geometries time-consuming, error prone, and tedious. Also, almost all NURBS models use trimming curves. Consequently, a global geometric discretization, based on NURBS, is usually not suitable as a basis for analysis.

T-splines were introduced in [39] in the CAGD community to address the fundamental limitations of NURBS. T-splines can model complicated engineering designs

as a single, watertight geometry. Additionally, NURBS are a special case of T-splines so existing technology based on NURBS extends to T-splines. Any trimmed NURBS model can be represented by a watertight trimless T-spline [40] and multiple NURBS patches can be merged into a single watertight T-spline [39, 41]. Unlike NURBS, T-splines can be locally refined [42, 43]. These geometric properties are especially critical in the context of boundary element methods where the behavior and accuracy of the method are strongly influenced by the watertightness, smoothness, and the ability to refine the surface mesh while maintaining exact geometry.

1.3. T-spline-based isogeometric analysis

Partnering T-spline discretizations with isogeometric analysis was first proposed in [44, 45] and described in detail in [46]. It was found that T-splines possess the same optimal convergence properties as NURBS with far fewer degrees-of-freedom. Later, *analysis-suitable* T-splines were formulated [47, 43]. Analysis-suitable T-splines are a canonical class of T-splines which possess the basic mathematical properties of NURBS (linear independence, partition of unity, etc.) while maintaining the local refinement property and design flexibility of general T-spline descriptions.

T-spline-based isogeometric analysis has been applied in various contexts. Application areas include fracture and damage [48, 49, 24], fluid-structure interaction [50], and shells [19]. A design-through-analysis framework utilizing immersed boundary methods, hierarchical refinement, and T-splines is described in [51]. Automatic conversion algorithms from unstructured quadrilateral and hexahedral meshes to T-splines surfaces and volumes is described in [38, 52]. Efficient and canonical finite element data structures for NURBS and T-splines based on Bézier extraction are described in [53, 54]. Mathematical studies of the basic approximation properties of analysis-suitable T-spline spaces are underway [55].

1.4. The boundary element method

The application of boundary integral equations in the context of engineering applications can be traced back to the early works of Jaswon [56] and Symm [57] for potential problems and then to elasticity by Cruse [58]. These early formulations outlined the key feature of the boundary element method (BEM): Discretization is restricted to the boundary of the physical domain. Free-space Green's functions (commonly referred to as fundamental solutions) for the specific problem class under consideration must be known *a priori* and singular integrals must be dealt with appropriately. Most often, in these early works, constant or linear elements were used to discretize the geometry and unknown solution fields. Later, isoparametric quadratic elements were used to minimize geometric and discretization errors [59]. Little has changed over the past few decades and discretizations using constant, linear or quadratic polynomials are predominant.

Several advances have been made which couple BEM and existing CAGD technologies in some form. In [60, 61], shape optimization is performed where NURBS are used for geometry representation and traditional polynomial basis functions are used to discretize the displacement and traction fields. The idea of combining BEM and IGA was first proposed in [2]. More recently, isogeometric boundary element analysis using NURBS curves and surfaces was developed in [62, 63, 64].

We note that there is a strong theoretical precedent for the use of T-spline discretizations (smooth splines), collocation-based boundary element methods, and exact geometry. In this context, several important asymptotic convergence estimates exist in $\mathbb{R}^2$ [65, 66] and to a more limited extent $\mathbb{R}^3$ [67, 68, 69].

T-spline surface designs and BEM form an ideal isogeometric partnership, as the main source of error in BEM is the geometrical approximation of the boundary representation, which is entirely eliminated by T-splines. We believe this represents one of the clearest instantiations of the IGA vision to date.

1.5. Structure and content of the paper

This paper is organized as follows. The boundary integral equations for linear elastostatics and accompanying fundamental solutions are presented in Section 2. Analysis-suitable T-splines, defined over unstructured grids, are then described in Section 3. Section 4 details the construction of the T-spline basis with emphasis placed on basis function definition near so called extraordinary points (vertices whose valence or the number of edges touching the vertex is not four). This constitutes the most comprehensive description of T-spline technology to date. A collocation approach, tailored to handle unstructured grids with T-junctions, is presented in Section 5. Sections 6 and 7 detail the discretization and collocation of the elastostatic boundary integral equations for both smooth and non-smooth boundaries, respectively. Numerical integration techniques which account for the singular integrals arising in the formulation are presented in Section 8. Finally, in Section 10, several demanding three-dimensional problems are solved, including a complete, exact T-spline model of a propeller.

Throughout this paper we use d_s and d_p to denote the number of spatial and parametric dimensions, respectively. In all cases, the polynomial degree p is 3. Spatial components of vectors and tensors are indexed by $i, j = 1, 2, \ldots, d_s$. We use n_{cp} to denote the number of T-spline basis functions and n_{cp}^e to denote the number of T-spline basis functions which are non-zero over element e.

2. Continuous boundary integral formulation

For an arbitrary physical domain, $\Omega \subset \mathbb{R}^{d_s}$, with boundary Γ, the boundary integral equation (BIE) for linear elastostatics, in the absence of body forces, is written as

$$\mathbf{C}(\mathbf{s})\mathbf{u}(\mathbf{s}) + \fint_\Gamma \mathbf{T}(\mathbf{s},\mathbf{x})\mathbf{u}(\mathbf{x})\,\mathrm{d}\Gamma(\mathbf{x}) = \int_\Gamma \mathbf{U}(\mathbf{s},\mathbf{x})\mathbf{t}(\mathbf{x})\,\mathrm{d}\Gamma(\mathbf{x}) \tag{1}$$

$$u_i(\mathbf{x}) = g_i(\mathbf{x}) \qquad \text{on } \Gamma_{g_i} \subseteq \Gamma \tag{2}$$

$$t_i(\mathbf{x}) = h_i(\mathbf{x}) \qquad \text{on } \Gamma_{h_i} \subseteq \Gamma \tag{3}$$

where $\mathbf{s} \in \Gamma$ is a boundary source point, $\mathbf{x} \in \Gamma$ is a boundary field point, $\mathbf{u}(\mathbf{x}) \in \mathbb{R}^{d_s}$ is the displacement vector at field point $\mathbf{x}$, $\mathbf{t}(\mathbf{x}) \in \mathbb{R}^{d_s}$ is the traction vector at field point $\mathbf{x}$, $\mathbf{U}(\mathbf{s},\mathbf{x}) = [U_{ij}]$ is a $d_s \times d_s$ real matrix representing the fundamental displacement kernel, $\mathbf{T}(\mathbf{s},\mathbf{x}) = [T_{ij}]$ is a $d_s \times d_s$ real matrix termed the fundamental traction kernel, and $\mathbf{C}(\mathbf{s}) = [C_{ij}]$ is a $d_s \times d_s$ real matrix called the jump term matrix (see Section 8.3 for additional details). We note that the jump term matrix only depends

on the geometric properties of the boundary at source point $\mathbf{s}$. If the source point lies on a smooth surface then $C_{ij} = \frac{\delta_{ij}}{2}$ where δ_{ij} is the kronecker delta. Due to the strong singularity in the fundamental traction kernel, $\mathbf{T}$, the integral associated with it is evaluated in the Cauchy Principal Value limiting sense (denoted by a dashed integral sign).

The fundamental displacement and traction kernels for two-dimensional domains are

$$U_{ij}(\mathbf{s},\mathbf{x}) = \frac{1}{8\pi\mu(1-\nu)}\left[(3-4\nu)\delta_{ij}\ln\frac{1}{r} + r_{,i}r_{,j}\right] \tag{4}$$

$$T_{ij}(\mathbf{s},\mathbf{x}) = -\frac{1}{4\pi(1-\nu)r}\left\{\frac{\partial r}{\partial \mathbf{n}}\left[(1-2\nu)\delta_{ij} + 2r_{,i}r_{,j}\right] + (1-2\nu)(n_i r_{,j} - n_j r_{,i})\right\} \tag{5}$$

and for three-dimensional domains the kernels are

$$U_{ij}(\mathbf{s},\mathbf{x}) = \frac{1}{16\pi\mu(1-\nu)r}\left[(3-4\nu)\delta_{ij} + r_{,i}r_{,j}\right] \tag{6}$$

$$T_{ij}(\mathbf{s},\mathbf{x}) = -\frac{1}{8\pi(1-\nu)r^2}\left\{\frac{\partial r}{\partial \mathbf{n}}\left[(1-2\nu)\delta_{ij} + 3r_{,i}r_{,j}\right] + (1-2\nu)(n_i r_{,j} - n_j r_{,i})\right\} \tag{7}$$

where $\mathbf{r} = \mathbf{x} - \mathbf{s}$, $r = |\mathbf{r}|$, $r_{,i} = \frac{\partial r}{\partial x_i}$, $\mathbf{n}$ is the unit outward normal evaluated at $\mathbf{x}$, n_i is its i^{th} component, μ is the shear modulus, and ν is Poisson's ratio.

3. Analysis-suitable T-splines over unstructured grids

To discretize the boundary integral equations (1) through (3) we define analysis-suitable T-splines over unstructured grids. This generalizes the notion of analysis-suitable T-splines described in [43, 47, 46]. Analysis-suitable T-splines preserve the important mathematical properties of NURBS while providing an efficient and highly localized refinement capability [43, 24]. All T-splines possess the following properties:

- The basis functions form a partition of unity.
- Each basis function is non-negative.
- An affine transformation of an analysis-suitable T-spline is obtained by applying the transformation to the control points. We refer to this as affine covariance; it is a consequence of the fact that the basis functions form a partition of unity. This implies that all patch tests (see [70]) are satisfied *a priori*.
- They obey the convex hull property. This is a consequence of partition of unity and non-negativity.
- Local refinement is possible.

However, not all T-splines have linearly independent basis functions [71]. It is shown in [47] that all T-splines whose T-meshes satisfy a simple topological condition do have linearly independent basis functions. T-splines that satisfy this topological requirement are called analysis-suitable T-splines [43, 46, 47]. Section 3.3 describes that topological requirement, and explains how it extends to T-meshes that have extraordinary points.

3.1. The unstructured T-mesh

An important object of interest underlying T-spline technology is the T-mesh, denoted by T. For surfaces, a T-mesh is a polygonal mesh and we will refer to the constituent polygons as elements or, equivalently, faces. Each element is a quadrilateral whose edges are permitted to contain T-junctions – vertices that are analogous to hanging nodes in finite elements. A control point, $\mathbf{P}_A \in \mathbb{R}^{d_s}$, and control weight, $w_A \in \mathbb{R}$, where the index A denotes a global control point number, is assigned to every vertex in the T-mesh.

The valence of a vertex, denoted by N, is the number of edges that touch the vertex. An extraordinary point is an interior vertex that is not a T-junction and for which $N \neq 4$. Edges that touch an extraordinary point are referred to as spoke edges.

The T-mesh elements which touch a T-mesh vertex form the one-ring neighborhood of the vertex. The two-ring neighborhood is the one-ring neighborhood and the elements that touch the one-ring neighborhood. An n-ring neighborhood is formed in the obvious way. We call the T-mesh elements and vertices contained in the two-ring neighborhood of an extraordinary point irregular elements and vertices, respectively. All other T-mesh elements and vertices are called regular elements and vertices. Figure 1 shows valence three and five extraordinary points, along with their one- and two-ring neighborhoods.

To define a basis, a valid knot interval configuration must be assigned to the T-mesh. A knot interval [72] is a non-negative real number assigned to an edge. A valid knot interval configuration requires that the knot intervals on opposite sides of every element sum to the same value. In this paper, we require that the knot intervals for spoke edges of an individual extraordinary point either be all non-zero or all zero.

3.2. T-junction extensions

A T-junctions extension consists of one or two directed line segments originating at the T-junction [43]. Figure 1 shows a T-mesh that contains a single T-junction, and the directed line segments in Figure 2a (drawn in dashed lines) are its extension. The black dashed line, extending over two faces, is called a face extension, and the portion of a face extension lying in the face immediately adjacent to the T-junction is called a one-bay face extension. The red dashed line, extending along a single edge, is called an edge extension. A T-junction lying on the boundary has a face extension but no edge extension. All other T-junctions have either one face extension and one edge extension, or two face extensions. The direction of an extension is always away from its T-junction. An extended T-mesh T_{ext} is formed by adding all T-junction extensions to a T-mesh T. Since T-junction extensions are closed line segments, a horizontal and vertical extension can intersect either on the interior of both extensions or at the endpoint of one extension or both extensions.

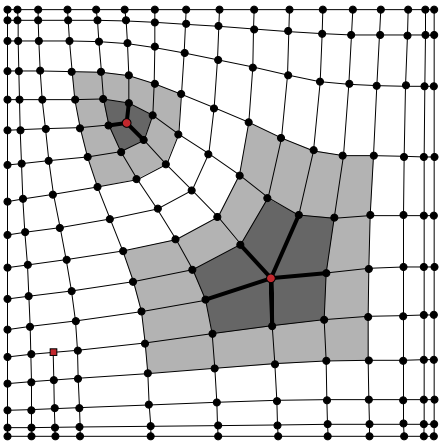

Figure 1: An unstructured T-mesh. Extraordinary points are denoted by red hollow circles and T-junctions are denoted by red hollow squares. The one-ring neighborhoods are composed of the darkly shaded elements and the two-ring neighborhoods are composed of the dark and lightly shaded elements. The spoke edges are denoted by the thick black lines.

3.3. Analysis-suitable definition

For T-meshes that have no extraordinary points, an analysis-suitable T-spline is defined in [47] to be one whose T-mesh has no intersecting extensions; it is proven in [47] that such T-splines have linearly independent basis functions. We now define an analysis-suitable T-spline with extraordinary points to be one whose T-mesh honors the following conditions: no T-junction extensions intersect, no one-bay face extension spans an element in the three-neighborhood of an extraordinary point, and no extraordinary point lies within the three-neighborhood of another extraordinary point. A proof is under development to assure that the basis functions for such T-splines are linearly independent. We use the adjective "analysis-suitable" to refer to a T-spline, and its T-mesh and extended T-mesh. The analysis-suitable extended T-mesh corresponding to the T-mesh in Figure 1 is shown in Figure 2a.

4. The unstructured T-spline basis

A T-spline basis function, N_A, is defined for every vertex, A, in the T-mesh. Each N_A is a bivariate piecewise polynomial function. If A has no extraordinary points in its two-neighborhood, N_A is comprised of a 4×4 grid of polynomials (see upper-right example in Figure 2d). Otherwise, the polynomials comprising N_A do not form a 4×4 grid (see the other two basis functions diagrammed in Figure 2d). In either case, the polynomials can be represented in Bézier form. Similarly, any T-spline can be decomposed into a finite set of Bézier elements and the set of T-spline control points maps linearly to the set of Bézier control points.

We note that the treatment and analysis of extraordinary points in control meshes that have quadrilateral faces has a rich history in CAGD. A popular approach in CAGD

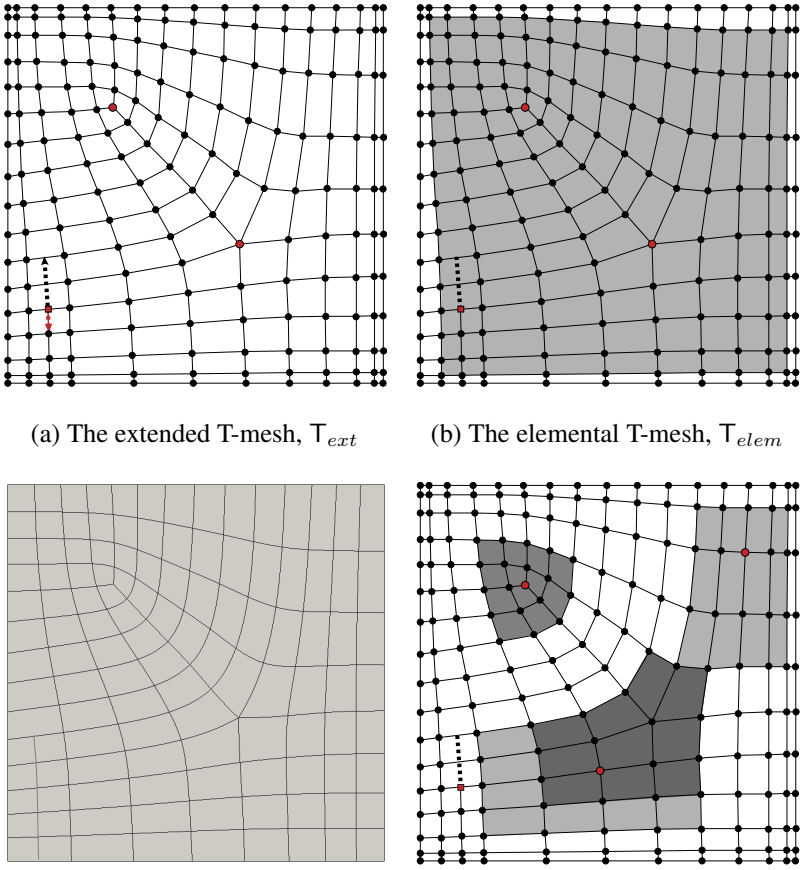

(a) The extended T-mesh, T_{ext}

(b) The elemental T-mesh, T_{elem}

(c) The Bézier Mesh

(d) Basis function supports in T_{elem}

Figure 2: The extended T-mesh, elemental T-mesh, Bézier mesh, and regular and irregular elemental supports of three particular T-spline basis functions. (a) The extended T-mesh, T_{ext}. The extended T-mesh is formed by adding all T-junction extensions to the T-mesh, T. In this case, there is a single T-junction extension shown on the left. The face extension is denoted by a black dashed arrow and the edge extension is denoted by a red dashed arrow. (b) The elemental T-mesh, T_{elem}. The elemental T-mesh, T_{elem}, is formed by adding all face extensions to T and then eliminating all elements for which the knot interval sum on any side is zero. The shaded elements are the elements in T_{elem}. (c) The Bézier mesh in physical space. The Bézier mesh is created through Bézier extraction as described in Section 4.2. (d) Three T-mesh vertices with the underlying sets of elemental T-mesh elements which support the corresponding basis functions. The lightly shaded rectangles are regular elements and the darkly shaded elements are irregular elements. In the top left, the basis function is supported entirely by irregular elements. In the top right, the basis function is supported entirely by regular elements. On the bottom, the basis function is supported by both regular and irregular elements. The portions of the basis functions supported by regular elements are B-splines while the portions supported by irregular elements are defined through the constrained optimization procedure described in Section 4.3.

to dealing with such extraordinary points is to use subdivision surfaces [73, 74, 75, 76, 77, 78, 79, 80]. In practice, the most popular approaches generalize uniform B-spline knot insertion, also known as h-refinement. Notable exceptions being NURSS [81] and T-NURCCs [39], which handle non-uniform knots and T-junctions, respectively. The subdivision process generates elements near the extraordinary point which are comprised of an *infinite* sequence of piecewise polynomials. We mention in passing that certain subdivision schemes have been used as a basis for finite element analysis [82, 83, 84, 85, 86].

As an alternative approach to dealing with extraordinary points, the CAGD community has increasingly explored *finite* polynomial representations for the surface surrounding an extraordinary point, typically with each control grid face mapping to a single polynomial patch. These approaches [87, 88, 89, 90, 91, 92, 93, 94, 95] are more amenable to real-time applications, modern GPU processors, and high-end engineering design where at least curvature continuity is required. In addition, in the context of T-splines, these constructions are both forward and backward compatible with NURBS, the current industry standard in CAD.

We focus our developments in this paper on defining the T-spline basis over irregular Bézier elements using one polynomial patch per element. We employ a constrained minimization framework which guarantees a specified level of smoothness and basic analysis-suitability properties. The construction of T-spline basis functions over regular Bézier elements is described in detail in [54].

4.1. The elemental T-mesh

An analysis-suitable elemental T-mesh, T_{elem}, is formed by adding all face extensions to T and then eliminating all elements for which the knot interval sum on any side is zero. A Bézier element is then associated with each element in T_{elem}. A Bézier element is a region of the T-spline surface in physical space bounded by knot lines. Each Bézier element has no interior knot lines, and hence can be represented by a single bivariate polynomial. We represent these polynomials in the Bernstein polynomial basis, so each Bézier element is a Bézier surface patch. Each knot line in physical space is the image of an edge in T_{elem}, or equivalently, a line of reduced continuity in at least one T-spline basis function. We call the collection of Bézier elements the Bézier mesh.

Figure 2b shows the elemental T-mesh corresponding to the T-mesh in Figure 1. The elements in the elemental T-mesh are shaded. A single face extension is included in T_{elem} denoted by a dashed line. Consistent with B-spline conventions, the outer ring of elements is always excluded from T_{elem}. These elements typically have at least one side whose knot intervals sum to zero to create an open knot vector structure along the boundary.

4.2. Bézier extraction

The Bézier elements in the Bézier mesh are defined through Bézier extraction. Recall that the set of T-spline control points maps linearly to the set of Bézier control points. This map allows us to "extract" the Bézier patches that comprise a T-spline. The transpose of this linear map is defined by a matrix called the extraction operator. In the context of finite element analysis, the extraction operator is a generalization of

the classical assembly operator and is used to standardize and localize element representation. In other words, the extraction operator maps a canonical tensor product Bernstein polynomial basis defined on Bézier elements to the global T-spline basis. The transpose of the extraction operator maps T-spline control points to the Bézier control points. See [53, 54] for a detailed description of Bézier extraction including the implementation of Bézier extraction into finite element codes.

4.3. Irregular Bézier element definition

Unlike regular Bézier elements, irregular Bézier elements cannot be defined through B-spline knot insertion. Instead, their control points are chosen to satisfy geometric constraints that create an attractive surface and satisfy basic analysis-suitability properties such as patch tests [46]. There are numerous applications of these constraints, and several papers have been written exploring various choices [87, 88, 89, 90, 91, 92, 93, 94, 95].

In this paper, we present a general framework for irregular Bézier element definition that can be applied to all constructions that produce a linear map from T-spline control points to Bézier control points. We also present a particular construction which is relatively simple to understand and implement.

The irregular Bézier elements produced by our construction honor the following conditions: Two-neighborhood elements are C^2 with adjoining three-neighborhood elements, and C^1 with their other neighbors; and one-neighborhood elements are G^1 (i.e., tangent plane continuous) with adjoining one-neighborhood elements and C^1 with adjoining two-neighborhood elements. One-neighborhood elements are biquartic Bézier patches. These conditions leave extra degrees of freedom which are satisfied by imposing a simple fairing functional to produce an aesthetically pleasing surface. The details of the construction, including the derivation of the G^1 constraints, written in terms of biquartic Bézier elements, and the simple fairing functional employed in this paper are presented in Appendix A and Appendix B.

4.3.1. A T-spline to Bézier transformation

The first step in our construction defines one bicubic Bézier element for each one- and two-neighborhood face in the control mesh. The control points of these bicubic elements are linear combinations of T-spline control points, and the coefficients of the linear combinations are rational polynomial functions of knot intervals, described in Appendix A with reference to Figure 3. We call the resulting linear transformation the T-spline to Bézier transformation. The two-neighborhood Bézier elements thus defined are C^1 with each other and C^2 with the adjoining three-neighborhood patches. The one-neighborhood Bezier elements are C^1 with the two-neighborhood patches, but only C^0 with each other. Since C^0 is not acceptable for most geometric modeling applications, some adjustments to the Bezier control points of the one-neighborhood elements must be made in order to achieve G^1 continuity.

Figure 4 shows the initial bicubic Bezier element control grids and basis functions resulting from the B-spline to Bézier transformation, corresponding to the two extraordinary points in Figure 1. Figure 5a shows the initial C^0 bicubic patches defining the basis function corresponding to the valence five extraordinary point in Figure 1. Notice the lack of smoothness.

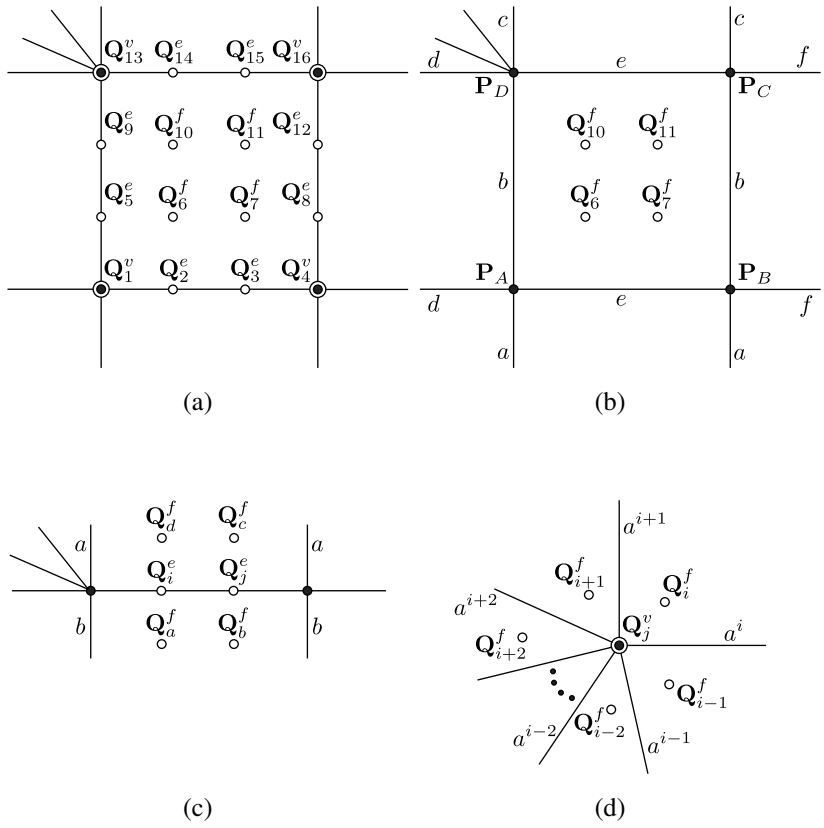

Figure 3: A non-uniform bicubic T-spline to Bézier transformation. (a) Face, edge, and vertex points defining an irregular Bézier element. The Bézier control points are denoted by open circles while the original T-spline control points are denoted by solid circles. Face Bézier points are denoted by a superscript f, edge Bézier points are denoted by a superscript e, and vertex Bézier points are denoted by a superscript v. Notice that the T-spline control points may or may not be extraordinary points. (b) Face points for a Bézier element (see Appendix A for detailed formulae). Each face point is written in terms of T-spline control points $\mathbf{P}_A$ through $\mathbf{P}_D$ and knot intervals a through f (see Appendix A for detailed formulae). (c) Edge points corresponding to an edge of an extraordinary element. Each edge point is written in terms of Bézier face points of neighboring Bézier elements and knot intervals a and b (see Appendix A for detailed formulae). (d) A vertex point corresponding to a corner of an extraordinary element. Each vertex point is written in terms of all adjacent face points and spoke edge knot intervals (see Appendix A for detailed formulae). Note that face points are defined first, followed by edge points, and finally vertex points.

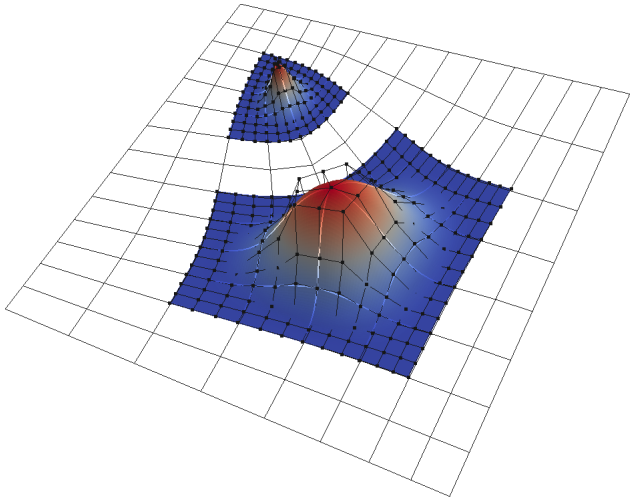

Figure 4: The initial bicubic Bézier element control grids and basis functions resulting from a B-spline to Bézier transformation, described in Section 4.3 and Appendix A, corresponding to the two extraordinary points in Figure 1. These basis functions do not lie in a portion of the T-mesh with a rectangular grid topology.

4.3.2. A constrained optimization framework

While it is possible to obtain G^1 continuity with bicubic patches, the resulting surface is quite rigid and does not allow inflection points in the curves adjacent to extraordinary points. To obtain a less rigid solution, we degree elevate the one-neighborhood elements to be biquartic, thereby providing additional degrees of freedom. We use most of these new degrees of freedom to enable a solution to the constraint equations that assure G^1 continuity. A few additional degrees of freedom remain, which are solved for by minimizing a fairing functional.

To be more precise, a constrained optimization problem can be solved for each T-spline basis function, N_A, in the two-neighborhood of a valence N extraordinary point. The T-spline to Bézier transformation, detailed in Appendix A, results in $\nu(N) = 20N + 1$ one-ring Bézier coefficients. We then assemble $\mu(N) = 40N$ fairing equations and $\tau(N) = 20N+1$ constraint equations, as described in Appendix B, into a fairing matrix $\mathbf{F}_A \in \mathbb{R}^{\mu(N)\times\nu(N)}$ and corresponding right-hand side $\mathbf{f}_A \in \mathbb{R}^{\mu(N)}$ and G^1 constraint matrix $\mathbf{G}_A \in \mathbb{R}^{\tau(N)\times\nu(N)}$ and corresponding right-hand side $\mathbf{g}_A \in \mathbb{R}^{\tau(N)}$, respectively. We can then find a vector of "smoothed" Bézier coefficients, $\tilde{\mathbf{c}}_A \in \mathbb{R}^{\nu(N)}$, which solves

$$\min_{\tilde{\mathbf{c}}_A \in \mathbf{S}_A} ||\mathbf{F}_A\tilde{\mathbf{c}}_A - \mathbf{f}_A||_2 \tag{8}$$

where

$$\mathbf{S}_A = \{\tilde{\mathbf{c}}_A \,|\, ||\mathbf{G}_A\tilde{\mathbf{c}}_A - \mathbf{g}_A||_2 = \min\}\,. \tag{9}$$

Once $\mathbf{F}_A$, $\mathbf{f}_A$, $\mathbf{G}_A$, and $\mathbf{g}_A$ are assembled we solve the constrained least squares problem using the method of direct elimination as described in [96]. This approach correctly handles any linear dependencies which may exist in the constraint matrix, $\mathbf{G}_A$. By solving a constrained optimization problem for each T-spline *basis function*, the smoothness is built into the basis. Consequently, the surface remains smooth for almost all control point configurations.

Figure 5b shows the T-spline basis function, comprised of G^1 biquartic patches, corresponding to the valence five extraordinary point in Figure 1. Figure 5a shows the initial C^0 bicubic patches. Notice the difference in smoothness.

4.4. The T-spline geometric map

Since both regular and irregular elements can be represented in Bézier form, a localized finite element representation of the global T-spline basis can be written using Bézier extraction and extraction operators. In other words,

$$\mathbf{N}^e(\tilde{\boldsymbol{\xi}}) = \mathbf{C}^e\mathbf{B}(\tilde{\boldsymbol{\xi}}) \tag{10}$$

where $\tilde{\boldsymbol{\xi}} \in \tilde{\Omega}$ is a coordinate in a standard parent element domain (see [70], Chapter 3, for a review of standard finite element paraphernalia, including the parent element domain), $\mathbf{N}^e(\tilde{\boldsymbol{\xi}}) = \{N_a^e(\tilde{\boldsymbol{\xi}})\}_{a=1}^{n_{cp}^e}$ is a vector of T-spline basis functions which are nonzero over element e, $\mathbf{B}(\tilde{\boldsymbol{\xi}}) = \{B_i(\tilde{\boldsymbol{\xi}})\}_{i=1}^{(p+1)^{d_p}}$ is a vector of tensor product Bernstein polynomial basis functions associated with Bézier element e, and $\mathbf{C}^e$ is the element extraction operator.

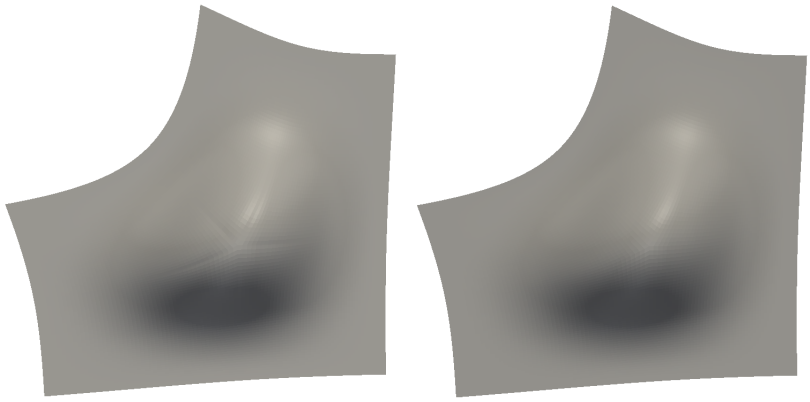

(a) (b)

Figure 5: The T-spline basis function corresponding to the valence five extraordinary point in Figure 1. (a) The C^0 bicubic patches whose control points are shown in Figure 4. (b) The G^1 biquartic patches

We can define the element geometric map, $\tilde{\mathbf{x}}^e : \tilde{\Omega} \rightarrow \Omega^e$, from the parent element domain onto the physical domain as

$$\tilde{\mathbf{x}}^e(\tilde{\boldsymbol{\xi}}) = \frac{1}{\left(\mathbf{w}^e\right)^T \mathbf{N}^e(\tilde{\boldsymbol{\xi}})} \left(\mathbf{P}^e\right)^T \mathbf{W}^e \mathbf{N}^e(\tilde{\boldsymbol{\xi}}) \tag{11}$$

$$= \left(\mathbf{P}^e\right)^T \mathbf{R}^e(\tilde{\boldsymbol{\xi}}) \tag{12}$$

where $\mathbf{R}^e(\tilde{\boldsymbol{\xi}}) = \{R_a^e(\tilde{\boldsymbol{\xi}})\}_{a=1}^{n_{cp}^e}$ is a vector of rational T-spline basis functions, the element weight vector $\mathbf{w}^e = \{w_a^e\}_{a=1}^{n_e}$, the diagonal weight matrix $\mathbf{W}^e = \mathrm{diag}(\mathbf{w}^e)$, and $\mathbf{P}^e$ is a matrix of dimension $n_{cp}^e \times d_s$ that contains element control points,

$$\mathbf{P}^e = \begin{bmatrix} P_1^{e,1} & P_1^{e,2} & \dots & P_1^{e,d_s} \\ P_2^{e,1} & P_2^{e,2} & \dots & P_2^{e,d_s} \\ \vdots & \vdots & & \vdots \\ P_{n_{cp}^e}^{e,1} & P_{n_{cp}^e}^{e,2} & \dots & P_{n_{cp}^e}^{e,d_s} \end{bmatrix}. \tag{13}$$

Using (11) and (12) we have that

$$\mathbf{R}^e(\tilde{\boldsymbol{\xi}}) = \frac{1}{\left(\mathbf{w}^e\right)^T \mathbf{N}^e(\tilde{\boldsymbol{\xi}})} \mathbf{W}^e \mathbf{N}^e(\tilde{\boldsymbol{\xi}}), \tag{14}$$

and using (10)

$$\mathbf{R}^e(\tilde{\boldsymbol{\xi}}) = \frac{1}{\left(\mathbf{w}^e\right)^T \mathbf{C}^e \mathbf{B}(\tilde{\boldsymbol{\xi}})} \mathbf{W}^e \mathbf{C}^e \mathbf{B}(\tilde{\boldsymbol{\xi}}). \tag{15}$$

Note that all quantities in (15) are written in terms of the Bernstein basis defined over the parent element domain, $\tilde{\Omega}$. The Bézier mesh in physical space corresponding to the T-mesh in Figure 1 is shown in Figure 2c. Each Bézier element is mapped into physical space using the T-spline geometric map (12).

5. Collocation

Collocation generates a set of discrete equations, that satisfy (1) through (3) exactly at a specified set of collocation points. Our collocation approach robustly handles T-junctions and extraordinary points. We first define n-ring local knot interval vectors and basis function domains and then describe how to compute the coordinates of collocation points in both parametric and physical space.

5.1. n-ring local knot interval vectors

An n-ring local knot interval vector, $\mathbf{K}_{A,n}$, is constructed from knot interval sequences inferred from the T-mesh in the neighborhood of the associated vertex, A. We construct an n-ring local knot interval vector, $\mathbf{K}_{A,n} = \{K^i_{A,n}\}_{i=1}^N$, where $K^i_{A,n} = \{k^i_{A,1}, k^i_{A,2}, \ldots, k^i_{A,n}\}$, by marching through the T-mesh in each topological direction, $i = 1, \ldots, N$, where N is four for ordinary vertices and equal to the number of spoke edges (i.e., valence) if the vertex is extraordinary, starting at vertex A, until n vertices or perpendicular edges are intersected. At each intersection, the knot interval distance traversed from the last intersection is placed in the local knot interval vector. If a T-mesh boundary is crossed or an extraordinary point is encountered before n knot intervals are constructed, it is common practice to set the remaining knot intervals to zero. We note that, for cubic T-splines, 2-ring local knot interval vectors can be constructed for each regular vertex in the T-mesh. These local knot interval vectors are used to construct T-spline basis functions. See [39, 54, 43] for additional details on T-spline basis function definition for regular T-mesh vertices. In this paper, 1-ring and 2-ring local knot interval vectors are also used to compute collocation points.

Figure 6 shows the 2-ring local knot intervals corresponding to an ordinary (a) and extraordinary vertex (b). For the ordinary vertex, we have that

$$\mathbf{K}_{A,2} = \left\{ \left\{k^1_{A,1}, k^1_{A,2}\right\}, \left\{k^2_{A,1}, k^2_{A,2}\right\}, \ldots, \left\{k^4_{A,1}, k^4_{A,2}\right\} \right\} \tag{16}$$

and for the valence five extraordinary vertex we have that

$$\mathbf{K}_{A,2} = \left\{ \left\{k^1_{A,1}, k^1_{A,2}\right\}, \left\{k^2_{A,1}, k^2_{A,2}\right\}, \ldots, \left\{k^5_{A,1}, k^5_{A,2}\right\} \right\}. \tag{17}$$

5.2. n-ring local basis function domains

When the T-mesh vertex is an ordinary point we use $\mathbf{K}_{A,n}$ to define a single local basis function domain, $\widehat{\Omega}_{A,n} \subset \mathbb{R}^2$, as

$$\widehat{\Omega}_{A,n} = \bigotimes_{i=1}^{2} \widehat{\Omega}^i_{A,n}, \tag{18}$$

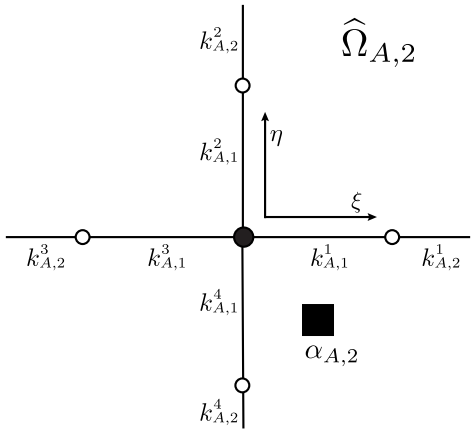

(a) 2-ring notation, ordinary case

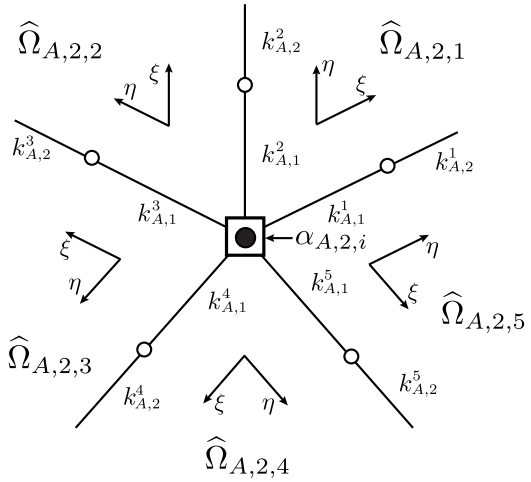

(b) 2-ring notation, extraordinary case

Figure 6: Collocation data corresponding to the 2-ring of both extraordinary and ordinary vertices. (a) Collocation data corresponding to the 2-ring of an ordinary vertex. (b) Collocation data corresponding to the 2-ring of a valence five extraordinary vertex.

where $\widehat{\Omega}^1_{A,n} = [-\sum_{j=1}^{n} k^3_{A,j}, \sum_{j=1}^{n} k^1_{A,j}]$ and $\widehat{\Omega}^2_{A,n} = [-\sum_{j=1}^{n} k^4_{A,j}, \sum_{j=1}^{n} k^2_{A,j}]$. A coordinate system, $\boldsymbol{\xi}_{A,n} = (\xi^1_{A,n}, \xi^2_{A,n}) = (\xi_{A,n}, \eta_{A,n})$, called the n-ring basis coordinate system, is assigned to each n-ring local basis function domain. Figure 6a shows the local basis function domain and 2-ring basis coordinate system for a ordinary vertex.

When the T-mesh vertex is extraordinary we use $\mathbf{K}_{A,n}$ to define a set of local basis function domains, $\left\{\widehat{\Omega}_{A,n,i}\right\}_{i=1}^{N}$, where $\widehat{\Omega}_{A,n,i} \subset \mathbb{R}^2$ is defined as

$$\widehat{\Omega}_{A,n,i} = \bigotimes_{j=1}^{2} \widehat{\Omega}^j_{A,n,i}, \tag{19}$$

where $\widehat{\Omega}^j_{A,n,i} = [0, \sum_{\ell=1}^{n} k^{i+j-1 \,(\mathrm{mod}\, N)}_{A,\ell}] \subset \mathbb{R}$. A coordinate system, $\boldsymbol{\xi}_{A,n,i} = (\xi^1_{A,n,i}, \xi^2_{A,n,i}) = (\xi_{A,n,i}, \eta_{A,n,i})$, called the i^{th} n-ring basis coordinate system, is assigned to each n-ring local basis function domain in the set. Figure 6b shows the five local basis functions domains and 2-ring basis coordinate systems for a valence five extraordinary vertex. Notice that the origin of each coordinate system is at the extraordinary vertex.

5.3. n-ring collocation points

To determine collocation points in the unstructured T-spline setting, we generalize the notion of Greville abscissae[1] to accomodate unstructured grids, T-junctions, and extraordinary points. Collocation at Greville abscissae has been shown to be an accurate choice in the context of collocated isogeometric boundary element [63, 64] and finite element methods [97, 98]. We note that, if the T-spline does not have T-junctions or extraordinary points, 1-ring collocation points described in this paper are equivalent to two-dimensional Greville abscissae. Additionally, we use 2-ring collocation points in the presence of discontinuous data. This ensures a unique location for each collocation point.

We associate an n-ring collocation point with each basis function (or, equivalently, control point). To determine the basis coordinates of an n-ring collocation point associated with a ordinary vertex we use the n-ring local knot interval vectors, $\mathbf{K}_{A,n}$, and the n-ring local basis function domain, $\widehat{\Omega}_{A,n}$, and compute the location of the collocation point in the n-ring basis coordinate system as

$$\boldsymbol{\alpha}_{A,n} = \left\{ \begin{array}{c} \frac{\sum_{j=1}^{n} -(n-j+1)k^3_{A,j} + \sum_{j=1}^{n}(n-j+1)k^1_{A,j}}{2n+1} \\ \frac{\sum_{j=1}^{n} -(n-j+1)k^4_{A,j} + \sum_{j=1}^{n}(n-j+1)k^2_{A,j}}{2n+1} \end{array} \right\}. \tag{20}$$

The basis coordinates for the 2-ring collocation point corresponding to the ordinary

[1] In CAGD, Greville abscissae commonly refer to particular control point positions in physical space which induce a linear geometric map. In this work, we instead use the term to refer to locations in parametric space computed from sequences of knot intervals and allow the geometric map to remain arbitrary.

vertex in Figure 6a is

$$\boldsymbol{\alpha}_{A,2} = \left\{ \begin{array}{c} \frac{2k^1_{A,1}+k^1_{A,2}-2k^3_{A,1}-k^3_{A,2}}{5} \\ \frac{2k^2_{A,1}+k^2_{A,2}-2k^4_{A,1}-k^4_{A,2}}{5} \end{array} \right\}, \tag{21}$$

which is denoted by the black square in Figure 6a.

The basis coordinates, in each n-ring local basis function domain, of an n-ring collocation point associated with an extraordinary vertex is simply

$$\boldsymbol{\alpha}_{A,n,i} = \{0,0\}^T, \quad i = 1, \ldots, N. \tag{22}$$

This choice is made for simplicity and because, for the case of a uniform knot interval configuration, it represents a strict generalization of the Greville abscissae to the unstructured setting.

Once the location of a collocation point has been determined in terms of an underlying n-ring basis coordinate system and basis function domain it is a simple matter to determine which Bézier element domain(s) contains the collocation point. The location of the collocation point in physical space is the image of the collocation point in the Bézier element domain under the T-spline geometric map (12).

6. Discretization for smooth boundaries

We first describe the T-spline discretization scheme used to solve (1) through (3) when the T-spline surface Γ is smooth. A smooth boundary is defined to be a surface with a continuous normal field. In this setting, both the displacement and traction fields are continuous. We describe necessary modifications for non-smooth boundaries in Section 7. In the smooth case, we discretize both displacements and tractions using the same set of T-spline basis functions. In other words,

$$\mathbf{u}(\mathbf{x}) = \sum_{A=1}^{n_{cp}} \mathbf{u}_A R_A(\mathbf{x}) \tag{23}$$

$$\mathbf{t}(\mathbf{x}) = \sum_{A=1}^{n_{cp}} \mathbf{t}_A R_A(\mathbf{x}) \tag{24}$$

where n_{cp} is the number of control points or T-mesh vertices in the T-mesh and R_A is a (rational) T-spline basis function as described in Section 4. Inserting (23) and (24)

into (1) through (3) gives

$$\sum_{A=1}^{n_{cp}} \mathbf{C}(\mathbf{s}) R_A(\mathbf{s}) \mathbf{u}_A + \sum_{A=1}^{n_{cp}} \fint_\Gamma \mathbf{T}(\mathbf{s},\mathbf{x}) R_A(\mathbf{x})\, \mathrm{d}\Gamma(\mathbf{x}) \mathbf{u}_A = \sum_{A=1}^{n_{cp}} \int_\Gamma \mathbf{U}(\mathbf{s},\mathbf{x}) R_A(\mathbf{x})\, \mathrm{d}\Gamma(\mathbf{x}) \mathbf{t}_A \tag{25}$$

$$\sum_{A=1}^{n_{cp}} R_A(\mathbf{s}) u_i^A = g_i(\mathbf{s}) \qquad \text{on } \Gamma_{g_i} \tag{26}$$

$$\sum_{A=1}^{n_{cp}} R_A(\mathbf{s}) t_i^A = h_i(\mathbf{s}) \qquad \text{on } \Gamma_{h_i} \tag{27}$$

where u_i^A and t_i^A are the i^{th} component of the displacement and traction control variables, respectively, associated with T-spline basis function R_A.

We now collocate (25) through (27) by specifying n_{cp} collocation points in Γ. In the smooth setting, we use 1-ring collocation points for both extraordinary and ordinary vertices. In other words, the collocation points, $\mathbf{s}_B \in \Gamma$, are computed using (20) for ordinary vertices and (22) for extraordinary vertices and then mapped into physical space using (12). Collocating (25) through (27) yields the set of equations

$$\sum_{A=1}^{n_{cp}} \mathbf{C}(\mathbf{s}_B) R_A(\mathbf{s}_B) \mathbf{u}_A + \sum_{A=1}^{n_{cp}} \fint_\Gamma \mathbf{T}(\mathbf{s}_B,\mathbf{x}) R_A(\mathbf{x})\, \mathrm{d}\Gamma(\mathbf{x}) \mathbf{u}_A = \sum_{A=1}^{n_{cp}} \int_\Gamma \mathbf{U}(\mathbf{s}_B,\mathbf{x}) R_A(\mathbf{x})\, \mathrm{d}\Gamma(\mathbf{x}) \mathbf{t}_A,\ B = 1, 2, \ldots, n_{cp} \tag{28}$$

$$\sum_{A=1}^{n_{cp}} R_A(\mathbf{s}_B) u_i^A = g_i(\mathbf{s}_B) \qquad \forall B \text{ such that } \mathbf{s}_B \in \Gamma_{g_i} \tag{29}$$

$$\sum_{A=1}^{n_{cp}} R_A(\mathbf{s}_B) t_i^A = h_i(\mathbf{s}_B) \qquad \forall B \text{ such that } \mathbf{s}_B \in \Gamma_{h_i}. \tag{30}$$

The boundary integrals in (28) can be localized to element integrals over Bézier elements using standard techniques [70] and the Bézier extraction framework described in Section 4.2 and [53, 54]. The equations (28), (29), and (30) are then assembled into the following linear system

$$\mathbf{K}\mathbf{d} = \mathbf{f} \tag{31}$$

where $\mathbf{K} \in \mathbb{R}^{2n_{cp}d_s \times 2n_{cp}d_s}$, $\mathbf{f} \in \mathbb{R}^{2n_{cp}d_s}$, and $\mathbf{d}$ is the vector of unknown boundary displacements and tractions, respectively. We note that the matrix, $\mathbf{K}$, is in general dense and non-symmetric.

7. Discretization for non-smooth boundaries

Most engineering models of interest have sharp edges and corners. In this case, the displacement field is continuous but the traction field is discontinous due to disconti-

nuities in the normal field. Ignoring the differing regularity requirements for displacements and tractions in the discretization has a dramatic impact on the accuracy of the solution. See Appendix C for a motivating example and a detailed discussion of the differing methods employed in the boundary element literature to handle discontinuous tractions. Using T-splines, we can automatically locally refine the T-spline basis such that any discontinuities are appropriately accomodated.

7.1. The semi-discontinuous T-spline basis

To correctly model continuous displacements and discontinuous tractions we use the original T-spline basis to discretize the displacements and a locally refined T-spline basis to discretize the tractions. We call this locally refined basis the semi-discontinuous T-spline basis. To be more precise, the displacements and tractions are discretized as

$$\mathbf{u}(\mathbf{x}) = \sum_{A=1}^{n_{cp}} \mathbf{u}_A R_A(\mathbf{x}) \tag{32}$$

$$\mathbf{t}(\mathbf{x}) = \sum_{B=1}^{n^s_{cp}} \mathbf{t}_B R^s_B(\mathbf{x}) + \sum_{C=1}^{n^d_{cp}} \mathbf{t}_C R^d_C(\mathbf{x}) \tag{33}$$

where the semi-discontinuous basis is composed of n^s_{cp} continuous basis functions, R^s_B, and n^d_{cp} discontinuous basis functions, R^d_C. These functions are created through exact local refinement of the original polynomial T-spline basis [42, 43] as described in Section 7.1.1. We note that $n_{cp} \leq n^s_{cp} + n^d_{cp}$. If $n^d_{cp} = 0$, then the surface is smooth and local refinement is not necessary since there are no discontinuities in the traction field.

Once the appropriate semi-discontinuous basis has been constructed, we follow the discretization procedure described in Section 6 by inserting (32) and (33) into (1) through (3). However, we now collocate the resulting equations with $n^s_{cp} + n^d_{cp}$ collocation points in Γ. We associate 1-ring collocation points with each R^s_B and 2-ring collocation points with each R^d_C. This ensures that no collocation points lie on edges or corners or are coincident.

Note that in the presence of discontinuities we generate a larger collocation point set than is strictly required to collocate the continuous displacement field. In that case, our method collocates a displacement unknown multiple times and sums the result through the global assembly operation.

7.1.1. Semi-discontinuous local refinement

Semi-discontinuous local refinement is a special case of analysis-suitable local refinement described in [43]. The purpose of the local refinement step is to introduce discontinuities in the T-spline basis only where the traction field is discontinuous due to discontinuities in the normal field on the surface. The steps of the local refinement algorithm are:

Step 1 Compute the physical location of all 1-ring collocation points on the surface corresponding to the original T-spline basis.

Step 2 Compute the number of unique normals at each collocation point.

Step 3 If the number of unique normals at a collocation point is greater than 1, refine the original basis function associated with the collocation point. This generates a set of refined basis functions which are added to the set of discontinous basis functions. Otherwise, add the original basis function to the set of continuous basis functions.

Step 4 Set the control points of the refined basis functions equal to the original control point.

To refine a T-spline basis function whose associated collocation point has a non-unique normal we compute the 2-ring local knot interval vectors and consider the following cases:

1. The associated vertex is ordinary:

1a. If $k^1_{A,1} = k^3_{A,1} = 0$ and $k^2_{A,1} \neq 0$ or $k^4_{A,1} \neq 0$ create two refined basis functions whose 2-ring local knot interval vectors are

$$\mathbf{K}_{I,2} = \left\{\{0,0\}, \left\{k^2_{A,1}, k^2_{A,2}\right\}, \left\{k^3_{A,1}, 0\right\}, \left\{k^4_{A,1}, k^4_{A,2}\right\}\right\} \tag{34}$$

$$\mathbf{K}_{J,2} = \left\{\left\{0, k^1_{A,2}\right\}, \left\{k^2_{A,1}, k^2_{A,2}\right\}, \{0,0\}, \left\{k^4_{A,1}, k^4_{A,2}\right\}\right\}. \tag{35}$$

1b. If $k^2_{A,1} = k^4_{A,1} = 0$ and $k^1_{A,1} \neq 0$ or $k^3_{A,1} \neq 0$ create two refined basis functions whose 2-ring local knot interval vectors are

$$\mathbf{K}_{I,2} = \left\{\left\{k^1_{A,1}, k^1_{A,2}\right\}, \left\{0, k^2_{A,2}\right\}, \left\{k^3_{A,1}, k^3_{A,2}\right\}, \{0,0\}\right\} \tag{36}$$

$$\mathbf{K}_{J,2} = \left\{\left\{k^1_{A,1}, k^1_{A,2}\right\}, \{0,0\}, \left\{k^3_{A,1}, k^3_{A,2}\right\}, \left\{k^4_{A,1}, 0\right\}\right\}. \tag{37}$$

1c. If $k^1_{A,1} = k^2_{A,1} = 0$ and $k^2_{A,1} = k^4_{A,1} = 0$ create four refined basis functions whose 2-ring local knot interval vectors are

$$\mathbf{K}_{I,2} = \left\{\left\{0, k^1_{A,2}\right\}, \left\{0, k^2_{A,2}\right\}, \{0,0\}, \{0,0\}\right\} \tag{38}$$

$$\mathbf{K}_{J,2} = \left\{\left\{0, k^1_{A,2}\right\}, \{0,0\}, \{0,0\}, \left\{0, k^4_{A,2}\right\}\right\} \tag{39}$$

$$\mathbf{K}_{K,2} = \left\{\{0,0\}, \{0,0\}, \left\{0, k^3_{A,2}\right\}, \left\{0, k^4_{A,2}\right\}\right\} \tag{40}$$

$$\mathbf{K}_{L,2} = \left\{\{0,0\}, \left\{0, k^2_{A,2}\right\}, \left\{0, k^3_{A,2}\right\}, \{0,0\}\right\}. \tag{41}$$

2. The associated vertex is extraordinary of valence N. In this case, create N refined basis functions whose 2-ring local knot interval vectors are:

$$\mathbf{K}_{I,2} = \left\{\left\{0, k^i_{A,2}\right\}, \left\{0, k^{i+1}_{A,2}\right\}, \{0,0\}, \{0,0\}\right\}, \quad i = 1, \ldots, N. \tag{42}$$

8. Numerical integration

Inspection of the fundamental kernels (4) through (7) reveal that as $\mathbf{s} \to \mathbf{x}$ the expressions become singular where, more specifically, the 3D kernels of (6) and (7) are found to be *weakly singular* and *strongly singular*, respectively. Therefore, appropriate numerical integration techniques must be used for the integrals in (1). In general, the boundary integrals can be classified into three types:

- **Non-singular integrals**: The source point $\mathbf{s}$ and field point $\mathbf{x}$ lie sufficiently far apart such that the integrand is considered regular.
- **Nearly singular integrals**: The source point lies close to, but not on, the element containing the field point.
- **Singular integrals**: The source point lies on the same element as the field point.

In the present work, Gauss-Legendre quadrature is used to evaluate the non-singular integrals. Accurate evaluation of nearly singular and singular integrals is more challenging.

8.1. Nearly singular integrals

Near singular integration is an active area of research in the boundary element community. In all cases, an adaptive scheme, which accurately measures the "closeness" of the source point to the element in question, must be devised and an appropriate integration technique employed. In [59], near singular integration is achieved by subdividing the element into equal length subelements with the number of subelements related to a bound on integration error. Transformation techniques which reduce the singularity of the integral thus allowing conventional Gauss-Legendre quadrature to be used are also common [99, 100, 101]. Another approach is to transform the integral into a singular part that can be integrated analytically leaving a non-singular part that can be easily evaluated [102].

In this paper, we do not employ an adaptive integration scheme for nearly singular integrals but instead use the same sufficiently high Gauss-Legendre quadrature rule for both non-singular and nearly singular integrals such that integration error is suppressed. We recognize that in most cases this represents overkill in terms of integral evaluation and we plan on pursuing appropriate adaptive quadrature schemes for isogeometric boundary element analysis in a forthcoming paper.

8.2. Evaluation of the weakly singular $\mathbf{U}$ *kernel*

In 3D, the $\mathbf{U}$ kernel is of $O(1/r)$ and can be transformed into a regular integral through polar integration. Denoting the local polar coordinate system, centered at $\tilde{\boldsymbol{\xi}}_{\boldsymbol{s}}$ (the parent coordinate of source point $\mathbf{s}$ in element e), as $\tilde{\boldsymbol{\rho}} = (\rho, \theta)$, this is achieved in the following manner:

$$\int_{\tilde{\Omega}^e} \mathbf{U}(\mathbf{s}, \mathbf{x}(\tilde{\boldsymbol{\xi}})) R_a^e(\tilde{\boldsymbol{\xi}}) J(\tilde{\boldsymbol{\xi}}) \, \mathrm{d}\tilde{\boldsymbol{\xi}} = \int_0^{2\pi} \int_0^{\hat{\rho}(\theta)} \mathbf{U}(\mathbf{s}, \mathbf{x}(\tilde{\boldsymbol{\rho}})) R_a^e(\tilde{\boldsymbol{\rho}}) J(\tilde{\boldsymbol{\rho}}) J_\rho(\tilde{\boldsymbol{\rho}}) \rho \, \mathrm{d}\tilde{\boldsymbol{\rho}} \quad (43)$$

where $\hat{\rho}$ is the distance from the source point to the element boundary for a given θ and J_ρ is the Jacobian transformation from polar to parent coordinates. The inclusion of the term ρ on the right-hand side of (43) transforms the weakly singular integral into a regular integral and Gauss-Legendre quadrature can now be used for evaluation. In this work, the element is split into subelements as shown in Figure 7, where the number of subelements can vary from two to four, depending on the position of the source point $\tilde{\boldsymbol{\xi}}_{\boldsymbol{s}}$.

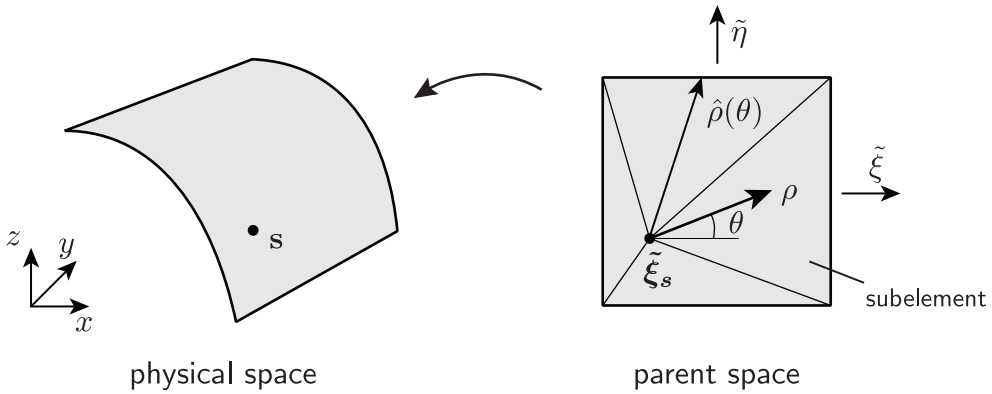

Figure 7: Definition of a polar coordinate system in the parent space of a Bézier element.

8.3. Evaluation of the strongly singular $\mathbf{T}$ *kernel*

The evaluation of the first integral of (28) often presents the most challenges since it involves the evaluation of a strongly singular integral. In addition, a byproduct of the CPV limiting process is the creation of the jump term, $\mathbf{C}$, which must be evaluated at each collocation point. In this work, the commonly used technique of rigid body motion [103], which can also be considered to be a form of regularized BEM [104], is used. It relies on the following expression:

$$\mathbf{C}(\mathbf{s}) = -\cancel{\int}_{\Gamma} \mathbf{T}(\mathbf{s},\mathbf{x})\,\mathrm{d}\Gamma(\mathbf{x}), \tag{44}$$

which is derived in Appendix D. By substituting this expression into (1), the following BIE is obtained:

$$\int_{\Gamma} \mathbf{T}(\mathbf{s},\mathbf{x})(\mathbf{u}(\mathbf{x}) - \mathbf{u}(\mathbf{s}))\,\mathrm{d}\Gamma(\mathbf{x}) = \int_{\Gamma} \mathbf{U}(\mathbf{s},\mathbf{x})\mathbf{t}(\mathbf{x})\,\mathrm{d}\Gamma(\mathbf{x}). \tag{45}$$

The integral on the left of (45) is now weakly singular and the technique described in Section 8.2 can be used. In practice, however, this integral is calculated in two separate parts. The discretized form of the first integral of (28), written as

$$\int_{\tilde{\Omega}^e} \mathbf{T}(\mathbf{s},\mathbf{x}(\tilde{\boldsymbol{\xi}}))R_a^e(\tilde{\boldsymbol{\xi}})J(\tilde{\boldsymbol{\xi}})\,\mathrm{d}\tilde{\boldsymbol{\xi}}, \tag{46}$$

is calculated for all elements (for a given source point $\mathbf{s}$), where the polar transformation described in Section 8.2 is used when $\tilde{\boldsymbol{\xi}}_{\boldsymbol{s}} \in \tilde{\Omega}^e$. These terms are placed in the

relevant matrix entries in (31). Next, by summing over the basis functions for a particular element and employing the partition of unity property of the (rational) T-spline basis, the following integral is calculated:

$$\sum_a \int_{\tilde{\Omega}^e} \mathbf{T}(\mathbf{s}, \mathbf{x}(\tilde{\boldsymbol{\xi}})) R_a^e(\tilde{\boldsymbol{\xi}}) J(\tilde{\boldsymbol{\xi}}) \, \mathrm{d}\tilde{\boldsymbol{\xi}} = \int_{\Omega^e} \mathbf{T}(\mathbf{s}, \mathbf{x}) \, \mathrm{d}\Omega^e. \tag{47}$$

Then, by accumulating the contributions given by (47) for each element, the jump term given by (44) is calculated at each collocation point. Since the point $\mathbf{s}$ is not guaranteed to lie at a point which is interpolated by the T-spline basis, the jump term must be multiplied by all the non-zero T-spline basis functions at the collocation point as shown in (28) and then placed in the final system of equations.

It should be noted, however, that by using the collocation strategy described in Section 7 for non-smooth boundaries, the jump term will always be of the form

$$\mathbf{C}(\mathbf{x}) = \frac{1}{2}\mathbf{I} \tag{48}$$

where $\mathbf{I}$ denotes the identity matrix. The reason for this is that all collocation points lie on smooth portions of the surface.

9. Evaluation of stresses

To evaluate stresses on the boundary using the boundary element method, two approaches can be used. In the first approach, a boundary integral equation is used directly by placing the collocation point at the desired location and integrating over the entire surface. This approach is accurate but requires hypersingular integration of the entire boundary. The second approach uses a combination of displacement derivatives and tractions, which are known at all points on the boundary (after analysis is performed). This approach is much more efficient than the first approach and is used in this paper. The accuracy of this approach is demonstrated in Section 10. The formulation is outlined in [105] and [106] but is summarised here for clarity.

To determine the boundary stress at a local element coordinate $(\tilde{\xi}, \tilde{\eta})$ and associated global coordinate $\mathbf{s}$ the tangent vectors and normal at this point are first computed as

$$\mathbf{m_1} = \frac{d\mathbf{x}}{d\tilde{\xi}}, \quad \mathbf{m_2} = \frac{d\mathbf{x}}{d\tilde{\eta}}, \quad \mathbf{n} = \mathbf{m_1} \times \mathbf{m_2}. \tag{49}$$

Note that this coordinate system may not be orthogonal. To determine an orthonormal coordinate system we compute

$$\mathbf{v_1} = \frac{\mathbf{m_1}}{|\mathbf{m_1}|}, \quad \mathbf{v_3} = \frac{\mathbf{n}}{|\mathbf{n}|}, \quad \mathbf{v_2} = \mathbf{v_3} \times \mathbf{v_1} \tag{50}$$

as shown in Figure 8.

To determine strains in the local orthonormal coordinate system, the displacement derivatives must be determined (Appendix E details the required formulae for $\partial u_1/\partial v_1$, $\partial u_2/\partial v_2$, $\partial u_1/\partial v_2$ and $\partial u_2/\partial v_1$). The local strains are defined in the standard way,

$$\varepsilon_{11} = \frac{\partial u_1}{\partial v_1}, \quad \varepsilon_{22} = \frac{\partial u_2}{\partial v_2}, \quad \varepsilon_{12} = \varepsilon_{21} = \frac{1}{2}\left(\frac{\partial u_1}{\partial v_2} + \frac{\partial u_2}{\partial v_1}\right). \tag{51}$$

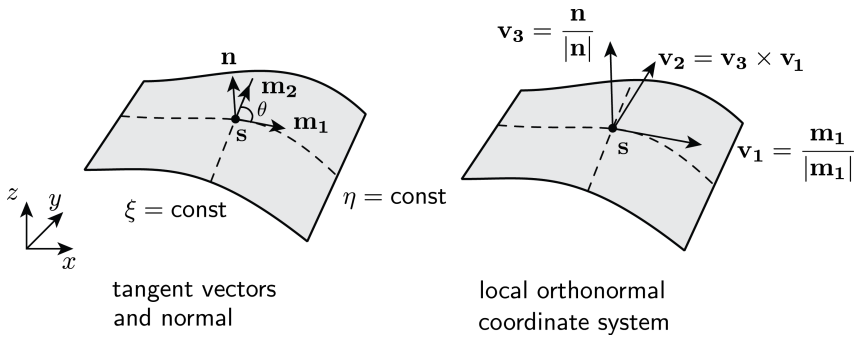

Figure 8: Representation of local tangent and normal vectors at a point $\mathbf{s}$ on an element, along with a local orthonormal coordinate system.

To determine stresses, the local strains, given by (51), and the traction at the point $(\tilde{\xi}, \tilde{\eta})$ must be known. The traction, written as

$$\mathbf{t}(\tilde{\boldsymbol{\xi}}) = \sum_{A=1}^{n_{cp}} \mathbf{t}_A R_A(\tilde{\boldsymbol{\xi}}), \tag{52}$$

can be transformed into the local coordinate system using a standard transformation matrix $\mathbf{R}$ (see Appendix E), i.e.,

$$\{\mathbf{t}_{local}\} = [\mathbf{R}]\,\{\mathbf{t}\}. \tag{53}$$

Local stresses can be computed from local strains and tractions as

$$\sigma_{11} = \frac{E}{1-\nu^2}(\varepsilon_{11} + \nu\varepsilon_{22}) + \frac{\nu}{1-\nu}\,t_3 \tag{54}$$

$$\sigma_{22} = \frac{E}{1-\nu^2}(\varepsilon_{22} + \nu\varepsilon_{11}) + \frac{\nu}{1-\nu}\,t_3 \tag{55}$$

$$\sigma_{12} = \frac{E}{1+\nu}\,\varepsilon_{12} \tag{56}$$

$$\sigma_{33} = t_3, \quad \sigma_{23} = \sigma_{32} = t_2, \quad \sigma_{13} = \sigma_{31} = t_1. \tag{57}$$

The stresses in the global coordinate system (x, y, z) can be computed as

$$\boldsymbol{\sigma} = [\mathbf{R}]^{\mathbf{T}}\,[\boldsymbol{\sigma}_{local}][\mathbf{R}]. \tag{58}$$

To determine interior stresses, a collocation point is placed at an interior point and the following boundary integral is evaluated [105, 106]

$$\sigma_{ij}(\mathbf{s}) + \int_\Gamma S_{kij}(\mathbf{s}, \mathbf{x}) u_k(\mathbf{x})\,\mathrm{d}\Gamma(\mathbf{x}) = \int_\Gamma D_{kij}(\mathbf{s}, \mathbf{x}) t_k(\mathbf{x})\,\mathrm{d}\Gamma(\mathbf{x}) \tag{59}$$

where the boundary displacement and traction components u_k, t_k are assumed to be known and S_{kij}, D_{kij} are given by

$$\begin{aligned} S_{kij} =& \frac{\mu}{4\pi(1-\nu)} \frac{1}{r^3} \Bigg(3\frac{\partial r}{\partial n}[(1-2\nu)\delta_{ij}r_{,k} + \nu(\delta_{ik}r_{,j} + \delta_{jk}r_{,i}) - 5r_{,i}r_{,j}r_{,k}] \\ & + 3\nu(n_i r_{,j} r_{,k} + n_j r_{,i} r_{,k}) + (1-2\nu)(3n_k r_{,i} r_{,j} + n_j\delta_{ik} + n_i\delta_{jk}) \\ & - (1-4\nu)n_k\delta_{ij} \Bigg) \end{aligned} \tag{60}$$

$$D_{kij} = \frac{1}{8\pi(1-\nu)r^2} \Bigg((1-2\nu)(\delta_{ik}r_{,j} + \delta_{jk}r_{,i} - \delta_{ij}r_{,k}) + 3r_{,i}r_{,j}r_{,k} \Bigg) \tag{61}$$

with summation implied over the repeated index k.

10. Numerical results

In this section we investigate the performance of T-spline-based isogeometric boundary element analysis. All geometries are discretized using bicubic T-spline basis functions. In the presence of sharp corners and edges a semi-discontinuous T-spline basis is used to discretize the tractions (see Section 7). The numerical computation for all the models is performed using the Bézier extraction framework described in Section 4.2. In all cases, the T-spline models were designed using the T-splines for Rhino plugin [107].

10.1. Patch tests

To study the behavior of our method, we first perform standard patch tests [108, 70]. In finite element methods, patch tests are used to determine whether an arbitrary "patch" of elements can exactly reproduce basic constant and linear deformation states. From a more practical standpoint, patch tests are also used to assess the correctness of a finite element implementation. They are also a valuable tool to assess the behavior of boundary element methods for similar reasons. Additionally, in the context of boundary element methods, they test the ability of the semi-discontinuous basis to accurately capture the discontinuous traction field, the correctness and accuracy of the underlying numerical integration routines, and the stability of the collocation scheme.

The patch test we consider is illustrated in Figure 9. Other standard patch tests such as shear and rotation are also satisfied by our method but are not shown for the sake of brevity. The origin of the physical coordinate system is denoted by a solid circle. The boundary conditions that are applied to each face of the cube are listed on the right. A Poisson's ratio of 0.3 is assumed and Young's modulus, E, is $1e5$. Due to the non-zero Poisson's ratio a fully three-dimensional stress state develops in the cube. The analytical solution to this problem is a constant stress profile and a linear displacement field in x, y, and z.

Three T-spline models of the cube are analyzed. These models are shown in Figure 10. The control points positions are shown on the left while the collocation point positions are shown on the right. The first T-mesh on the top left consists of 6 Bézier

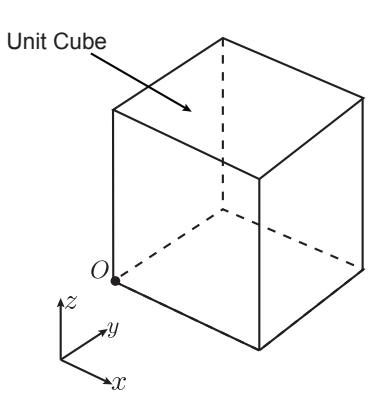

$x=0$ face:	$x=1$ face:
$u_x = 0$	$u_x = 0.1$
$t_y = 0$	$t_y = 0$
$t_z = 0$	$t_z = 0$
$y=0$ face:	$y=1$ face:
$t_x = 0$	$t_x = 0$
$u_y = 0$	$t_y = 0$
$t_z = 0$	$t_z = 0$
$z=0$ face:	$z=1$ face:
$t_x = 0$	$t_x = 0$
$t_y = 0$	$t_y = 0$
$u_z = 0$	$t_z = 0$

Figure 9: A three-dimensional patch test. The boundary conditions which are applied to each face of the cube are listed on the right. Due to the non-zero Poisson's ratio a fully three-dimensional stress state develops in the cube. The analytical solution to this problem is a constant stress profile and a linear displacement field in x, y, and z.

elements and 56 control points, the second T-mesh in the middle left consists of 96 Bézier elements and 218 control points, and the last T-mesh on the bottom left consists of 180 Bézier elements and 310 control points. The T-mesh on the bottom contains T-junctions which results in an unstructured collocation point configuration as shown on the bottom right. In all cases, and to minimize integration error, a 20×20 Gauss quadrature rule is used in each Bézier element to integrate both singular, nearly singular, and non-singular integrals. We note that the eight corner points are extraordinary points of valence three. We mention in passing that patch tests were also performed where several elements were distorted by moving control points. In all cases, the patch tests were satisfied.

The results for the patch test are shown in Figure 11. In all cases, a linear displacement profile in x, y, and z and constant stress profile are achieved by the method. The results were indistinguishable for the three T-splines shown in Figure 10 which indicates that the collocation point location scheme and semi-discontinuous T-spline discretization are robust and accurate even in the presence of T-junctions. Only the traction in x is shown. The tractions in y and z are not shown since they are identical up to integration error which in this case was $O(10^{-8})$. Using a higher order Gauss rule eliminates these errors. Note that the computed traction in the x-direction on x-faces is constant whereas it was set to zero on y- and z-faces. This is facilitated by the discontinuous treatment of tractions across sharp edges.

10.2. Solid circular cylinder subjected to internal pressure loading

The problem of a solid circular cylinder subjected to an internal pressure loading is shown in Figure 12. The exact solution, in terms of displacement and stresses in polar

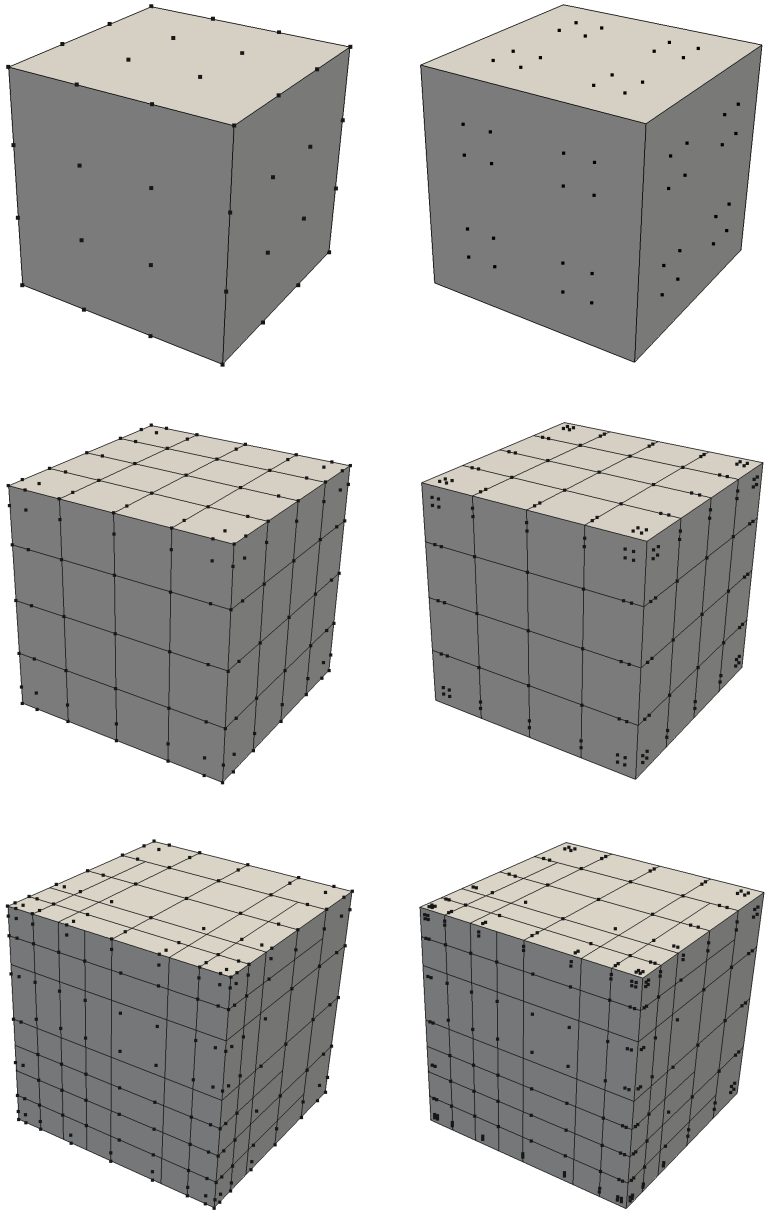

Control point positions Collocation point positions

Figure 10: Three T-spline models of the cube. The T-splines increase in complexity from top to bottom. On the left, the control point positions are shown. On the right, the collocation point positions are shown. Notice that the collocation point positions for the T-spline model on the bottom right are unstructured, mirroring the unstructured nature of the underlying T-mesh (i.e., there are T-junctions in the T-mesh). In all cases, the extracted Bézier meshes are also shown.

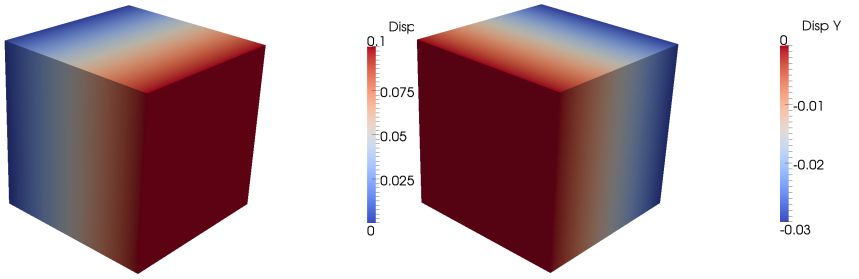

Displacement in x Displacement in y

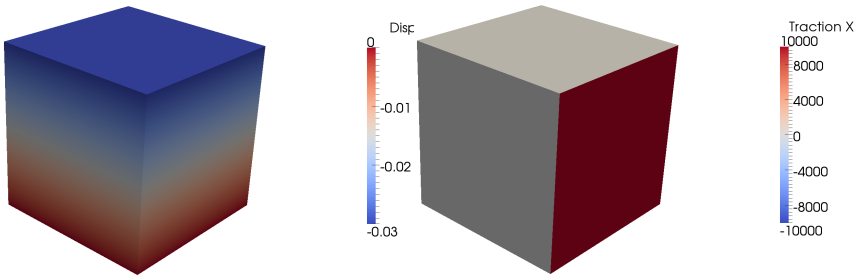

Displacement in z Traction in x

Figure 11: Results for the patch test described in Figure 9 for the three different T-spline models shown in Figure 10. For the three T-splines the results are indistinguishable. Note that the computed traction in the x-direction on x-faces is constant whereas it was set to zero on y- and z-faces.

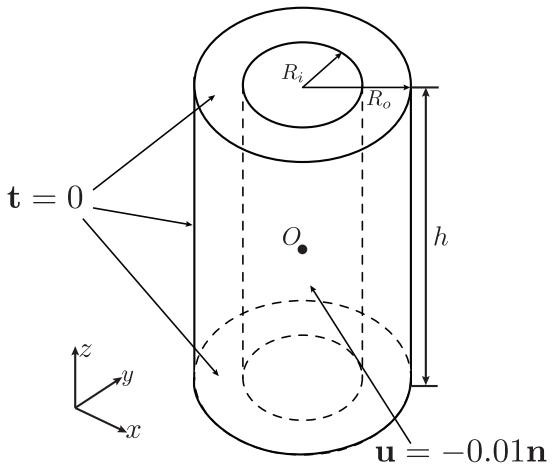

Figure 12: A thick cylinder pressurized internally.

coordinates (R, θ), for the case with constant pressure, is

$$u_R(R) = \frac{1}{E}\frac{PR_i^2}{R_o^2 - R_i^2}\left((1-\nu)R + \frac{R_o^2(1+\nu)}{R}\right) \tag{62}$$

$$\sigma_{RR}(R) = \frac{PR_i^2}{R_o^2 - R_i^2} - \frac{PR_i^2R_o^2}{R^2(R_o^2 - R_i^2)} \tag{63}$$

$$\sigma_{\theta\theta}(R) = \frac{PR_i^2}{R_o^2 - R_i^2} + \frac{PR_i^2R_o^2}{R^2(R_o^2 - R_i^2)}, \tag{64}$$

where R_i is the radius of the inner cylinder, R_o is the radius of the outer cylinder, P is the pressure applied to the inner cylinder, E is Young's modulus, and ν is Poisson's ratio. A small normal displacement, denoted by $\mathbf{n}$ in Figure 12, is applied to the internal cylinder while zero traction is applied on all other surfaces.

We demonstrate the accuracy of the method by studying the behavior of the solution on the coarse T-spline model shown in Figure 13. This T-spline is an exact representation of the thickened cylinder shown in Figure 12 where $R_i = \frac{1}{2}$, $R_o = 1$, and $h = 4$. The origin of the physical coordinate system is denoted by a small solid circle. We take Young's modulus, E, as $1e5$ and Poisson's ratio, ν, as zero. The Bézier Mesh has 96 Bézier elements and 320 T-spline control points. A 30×30 Gauss quadrature rule is used to integrate each Bézier element.

The deformed configuration for the cylinder is shown in Figure 14a. The axisymmetric deformation of the cylinder is apparent. In Figure 14b, the maximum scaled error in radial displacement, $\frac{|u-u^h|}{||u||_\infty}$, is plotted. The maximum scaled error in radial displacement and pressure, $\frac{|p-p^h|}{||p||_\infty}$, are 0.00111565 and 0.000461453, respectively. Note

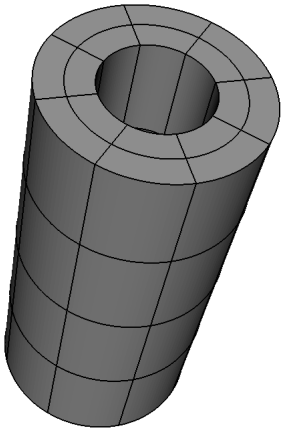

Figure 13: An exact T-spline model of the thickened circular cylinder in Figure 12. The extracted Bézier mesh is shown.

that the percent error for radial displacement is approximately 0.1% and the percent error for pressure is approximately 0.05%. This is remarkably accurate considering that the Bézier mesh consists of only 96 elements as shown in Figure 13. This demonstrates the potential of the method to obtain accurate analysis results during the design phase of the design-through-analysis iterative cycle, where, in most cases, the control mesh is kept as coarse as possible to facilitate the design process. If additional accuracy is required it can be obtained using T-spline local refinement.

The values of σ_{RR} along a radial line, $\theta = 0$, $R = 0.5$ to $R = 1.0$ are determined numerically and compared against the analytical solution for the T-spline shown in Figure 13. A 30×30 Gauss quadrature rule is used to integrate each Bézier element. The results are shown in Figure 15. Again, remarkable accuracy is obtained considering that there is only two Bézier elements through the thickness.

10.3. Spherical hole in an infinite domain subjected to uniform tension at $R = \infty$

The problem of a spherical hole in an infinite domain in $\mathbb{R}^3$ is shown in Figure 16. The exact solution, in terms of displacements in spherical coordinates (R, β, θ), is given

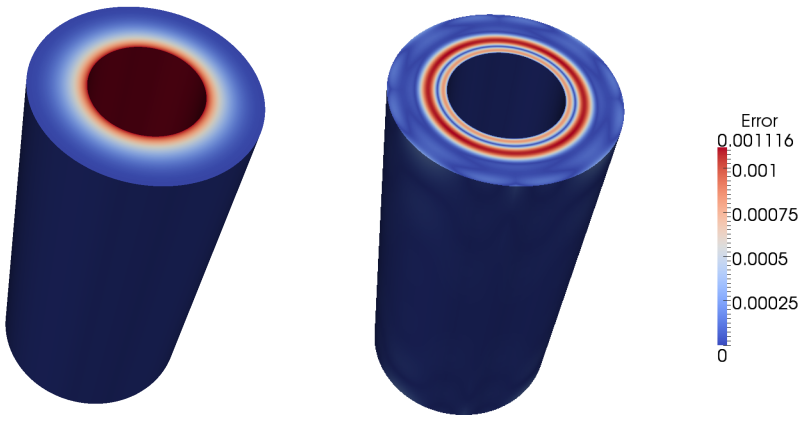

(a) (b)

Figure 14: (a) Radial displacement contours and (b) the errors in radial displacement, $\frac{|u-u^h|}{||u||_\infty}$.

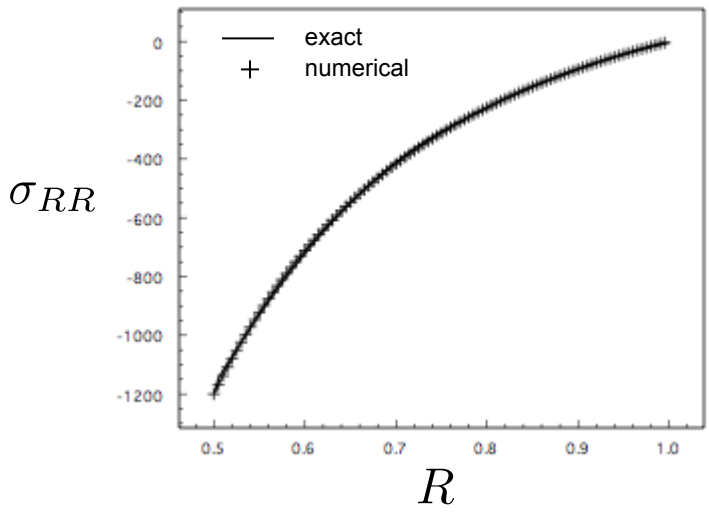

Figure 15: Numerical and analytical σ_{RR} for thick cylinder problem along radial line $R = 0.5$ to $R = 1.0$. Results are illustrated for the Bézier mesh in Figure 13.

by

$$2\mu u_R = -A_1 R + \frac{3A_2}{2R^4} - \frac{A_3}{R^2} \tag{65}$$
$$+ \left(3A_1 R - \frac{9A_2}{2R^4} + B_1(4\nu - 2)R + \frac{B_2(4\nu - 5)}{R^2}\right)\cos^2\beta$$
$$2\mu u_\beta = \left[-3A_1 R - \frac{3A_2}{R^4} + \left(B_1 R + \frac{B_2}{R^2}\right)(2 - 4\nu)\right]\sin\beta\cos\beta \tag{66}$$
$$u_\theta = 0 \tag{67}$$

where

$$A_1 = \frac{S\nu}{1+\nu}, \quad A_2 = \frac{Sa^5}{7-5\nu}, \quad A_3 = \frac{Sa^3(6-5\nu)}{2(7-5\nu)}, \tag{68}$$

$$B_1 = -\frac{S}{2(1+\nu)}, \quad B_2 = -\frac{5Sa^3}{2(7-5\nu)}, \tag{69}$$

a denotes the radius of the sphere, S is the uniaxial tension applied at infinity, μ is the shear modulus, and ν is Poisson's ratio. For completeness, the exact solution, in terms of stresses, is given by

$$\sigma_{RR} = S\cos^2\beta + \frac{S}{7-5\nu}\left(\frac{a^3}{R^3}(6 - 5(5-\nu)\cos^2\beta) + \frac{6a^5}{R^5}(3\cos^2\beta - 1)\right) \tag{70}$$
$$\sigma_{\theta\theta} = \frac{2}{2(7-5\nu)}\left(\frac{a^3}{R^3}(5\nu - 2 + 5(1-2\nu)\cos^2\beta) + \frac{a^5}{R^5}(1 - 5\cos^2\beta)\right) \tag{71}$$
$$\sigma_{\beta\beta} = S\sin^2\beta \tag{72}$$
$$+ \frac{S}{2(7-5\nu)}\left(\frac{a^3}{R^3}(4 - 5\nu + 5(1-2\nu)\cos^2\beta) + \frac{3a^5}{R^5}(3 - 7\cos^2\beta)\right)$$
$$\sigma_{R\beta} = S\left\{-1 + \frac{1}{7-5\nu}\left(-\frac{5a^3(1+\nu)}{R^3} + \frac{12a^5}{R^5}\right)\right\}\sin\beta\cos\beta. \tag{73}$$

The problem is modeled by placing the sphere in a cube and applying exact displacement boundary conditions to the faces of the cube and an exact (in this case, zero) traction boundary condition to the surface of the sphere, as shown in Figure 16.

The Bézier mesh for a coarse T-spline model of the problem in Figure 16 is shown in Figure 17, on the left. The Bézier mesh of the spherical hole is shown in Figure 17, on the right, where $a = \frac{1}{2}$. We take Young's modulus, E, as $1e5$ and Poisson's ratio, ν, as 0.3. The Bézier Mesh has 14 Bézier elements and 147 T-spline control points.

The T-spline sphere is created by degenerating a rectangular T-spline surface. The poles of the sphere are defined by multiple coincident control points. We note that the single T-spline basis function corresponding to a control point at one of the poles is defined to be the sum of all basis functions whose control points are coincident at that pole. This is a standard technique in finite elements for degenerate elements [70] and has been shown to produce basis functions which are in the Sobolev space H^1 [109] in the context of isogeometric analysis. A 20×20 Gauss quadrature rule is used to integrate each Bézier element.

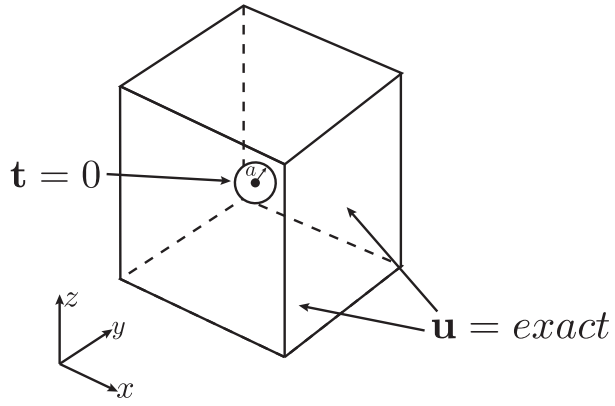

Figure 16: A spherical hole in an infinite domain in $\mathbb{R}^3$ subjected to uniform tension at $R = \infty$. The infinite domain is modeled by enclosing the sphere in a box and applying an exact displacement boundary condition to the faces of the box.

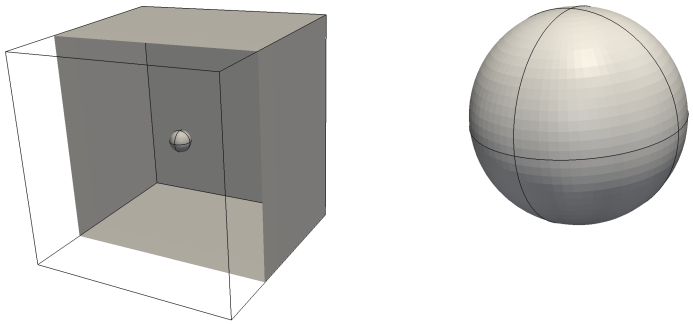

Figure 17: An exact T-spline model of the spherical hole enclosed in a cube (left) described in Figure 16. In all cases, the exact Bézier mesh is shown. The Bézier mesh of the sphere is shown on the right.

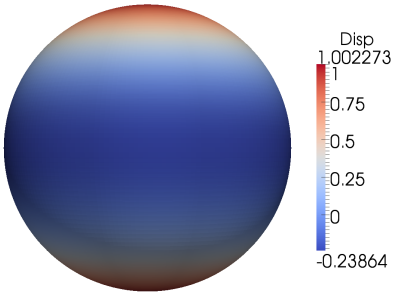

Exact displacement, u_R

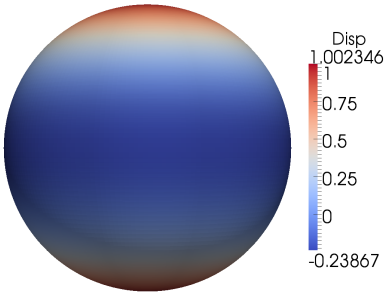

Computed displacement, u_R^h

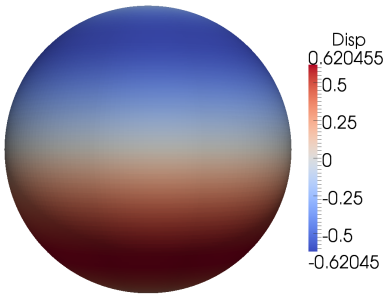

Exact displacement, u_β

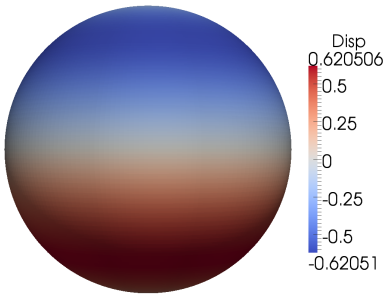

Computed displacement, u_β^h

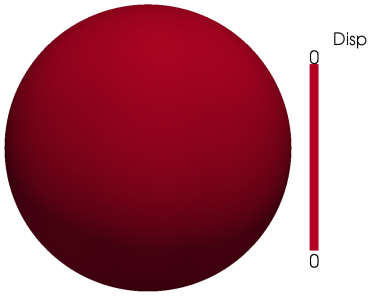

Exact displacement, u_θ

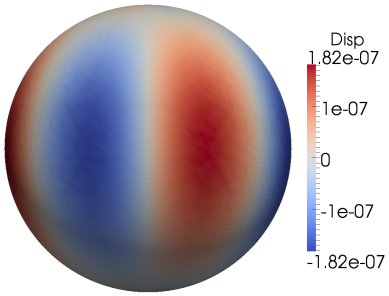

Computed displacement, u_θ^h

Figure 18: Exact displacements in R, β, and θ coordinates (left) compared with computed displacements (right).

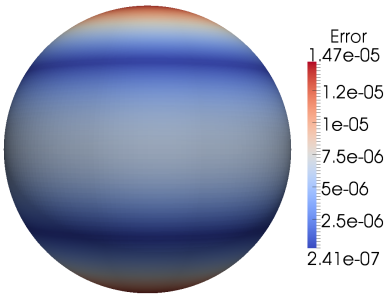

$\frac{|u_R - u_R^h|}{||u_R||_\infty}$

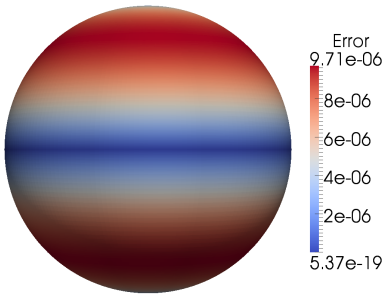

$\frac{|u_\beta - u_\beta^h|}{||u_\beta||_\infty}$

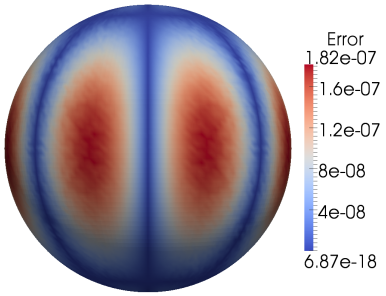

$\frac{|u_\theta - u_\theta^h|}{||u_\theta||_\infty}$

Figure 19: Errors in R, β, and θ displacements.

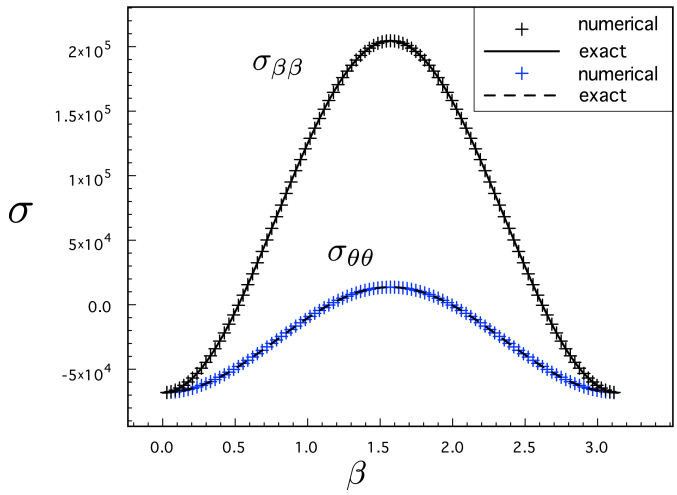

Figure 20: The values of spherical stress components along the line $0 \leq \beta \leq \pi$, $\theta = 0$ and $R = 0.5$. It should be noted that all other stress components are zero along this line.

Figure 18 shows the exact displacement solutions in R, β, and θ on the left, and the computed displacement solutions on the right. Figure 19 shows the error in displacements. The maximum scaled errors in the R, β, and θ displacements on the sphere are $1.47159e-5$, $9.70546e-6$, and $1.81719e-7$, respectively. Again, notice the accuracy of the solution. In this case, the sphere is discretized with only 8 Bézier elements.

The values of $\sigma_{\beta\beta}$ and $\sigma_{\theta\theta}$ along the line, $R = 0.5, \theta = 0, 0 \leq \beta \leq \pi$, are determined numerically and compared against the analytical solution for the T-spline shown in Figure 17. A 20×20 Gauss quadrature rule is used to integrate each Bézier element. The stress results are shown in Figure 20 where the exact and computed stresses are visually identical. We note that all other stress components are zero along this line.

10.4. A T-spline propeller

To illustrate the ability of the isogeometric boundary element method to handle complex engineering geometries, a T-spline propeller design is analyzed. The extracted Bézier mesh is shown in Figure 21. The entire geometry is a single T-spline consisting of $10,080$ control points and $10,080$ Bézier elements. Figure 22 shows a closeup of an unstructured section of the Bézier mesh. Notice the smooth Bézier elements surrounding each extraordinary point. These elements are constructed using the analysis-suitable irregular element construction described in Section 4. There are a total of 48 extraordinary points in the model.

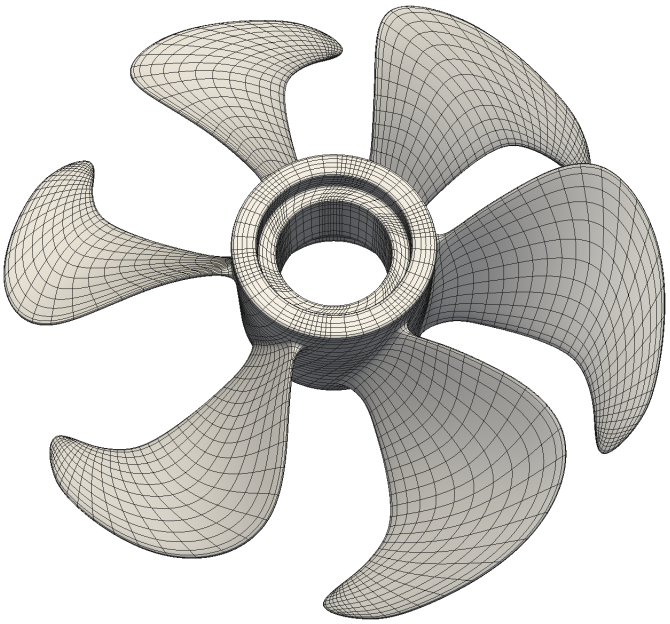

Figure 21: An extracted Bézier mesh for a propeller.

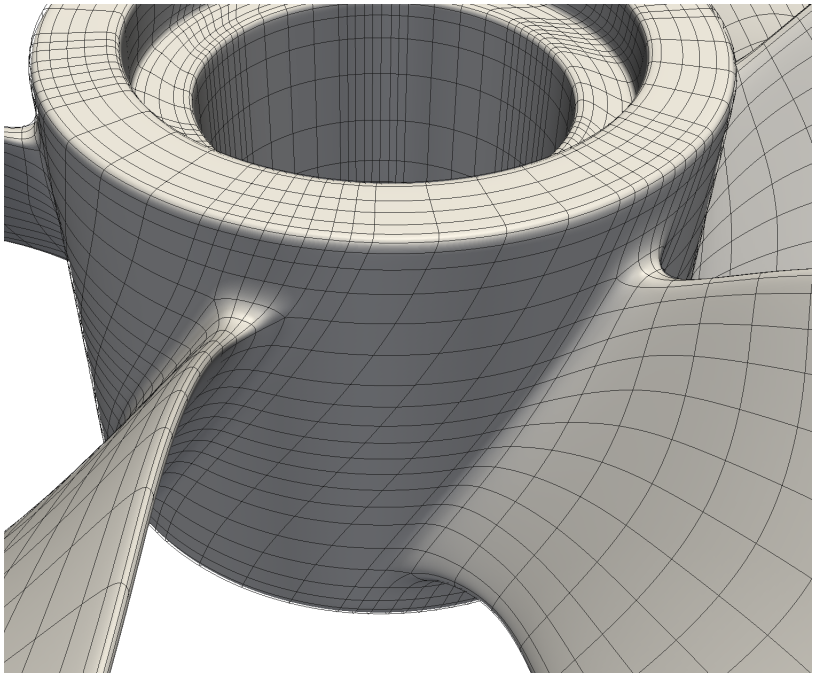

Figure 22: A closeup of a smooth unstructured region of the Bézier mesh. The transition between each propeller fin and the shaft is accomplished using four extraordinary points.

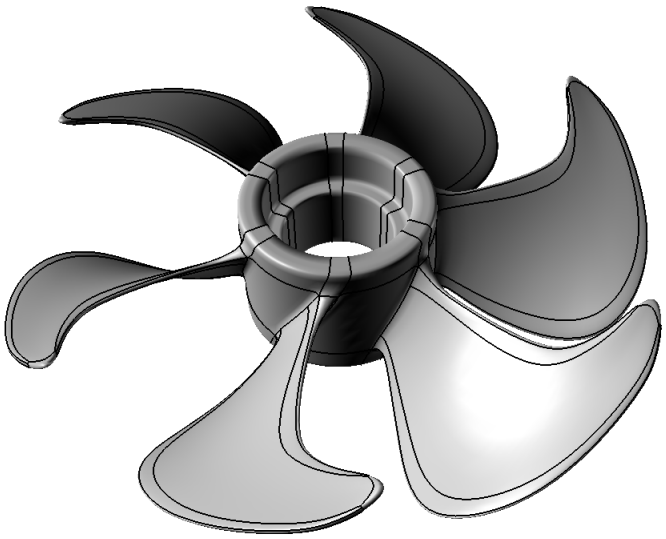

Figure 23: An equivalent 72 patch NURBS for the T-spline propeller in Figure 21.

To illustrate the importance of being able to accomodate extraordinary points in both design and analysis, an equivalent representation of the propeller as a multi-patch NURBS is shown in Figure 23. In this case, there are 72 NURBS patches. In the context of NURBS-based design, the propeller would be constructed patch-by-patch with smoothness across patches enforced (usually manual) by control point positioning. When used in analysis, all inter-patch connectivity and smoothness must be enforced explicitly in the analysis to ensure consistent (at least continuous) deformations of the geometry. This would be an enormous burden in analysis, but is completely eliminated with T-splines.

In the context of T-spline-based isogeometric analysis, extraordinary points are handled naturally and all smoothness considerations are built into the basis functions. These properties are transferred automatically to the analysis since the geometric basis is used as the basis for analysis.

We note that the the multi-patch NURBS shown in Figure 23 was generated automatically from the T-spline in Figure 21. This forward and backward compatibility between T-splines and NURBS is made possible, in large part, by the finite polynomial representation of the irregular Bézier elements surrounding each extraordinary point as described in Section 4. This would not be possible if a subdivision-based approach was being used near the extraordinary points.

Figure 24 shows the location of the collocation points in physical space for the propeller. The knot interval configuration (see Section 3) for the propeller is uniform so the collocation points are close to the corners of each Bézier element.

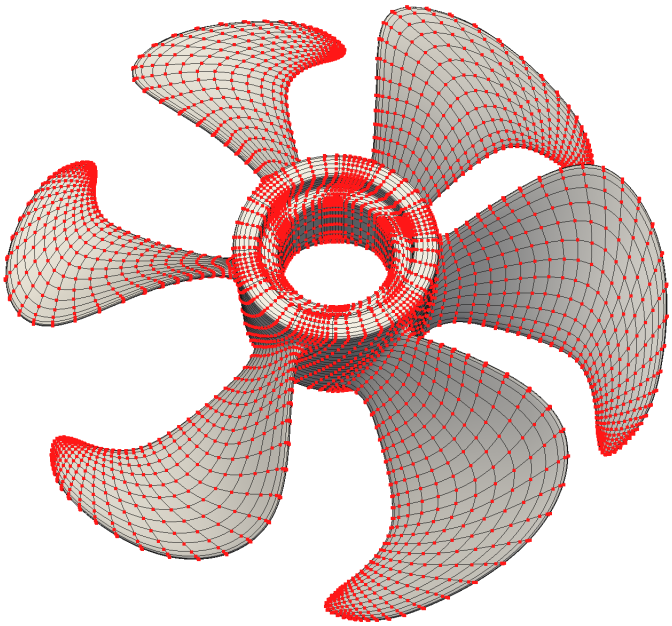

Figure 24: Collocation point locations in physical space for the propeller problem.

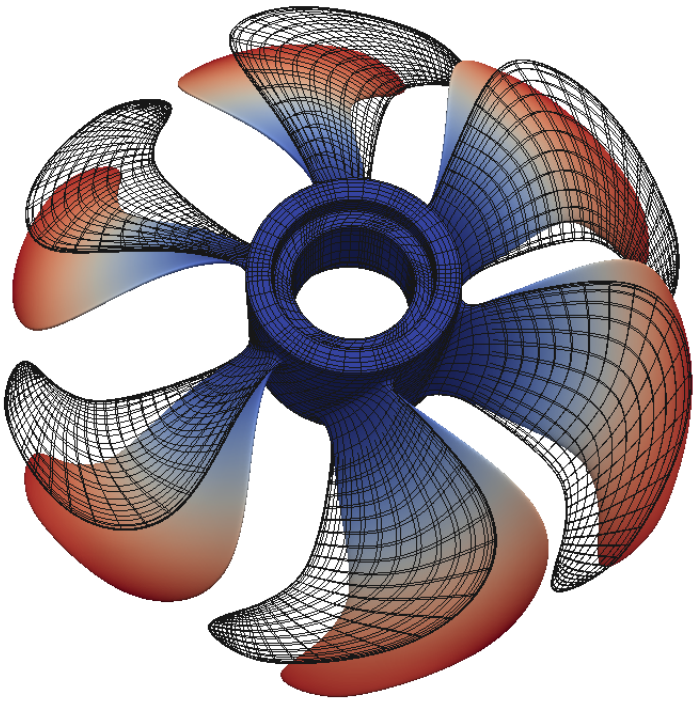

Figure 25: The original Bézier mesh for the propeller model and an exaggerated displacement profile with displacement magnitude superimposed.

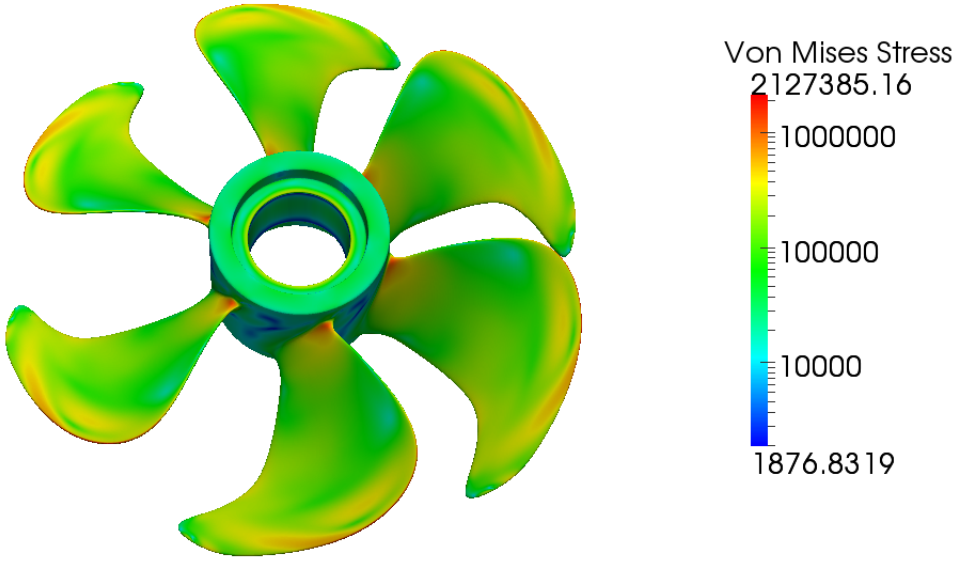

Figure 26: The von Mises stress solution for the T-spline propeller model. Note that a logarithmic scale is used to plot the stress.

A wind loading is simulated by setting all displacement components on the interior cylindrical surface to zero and setting the traction on all other surfaces to $\mathbf{t} = \{0, 0, -1000n_z\}^T$ if $n_z > 0$ and zero otherwise. We set Young's modulus, E, to $1e5$ and Poisson's ratio, ν, to 0.3. Figure 25 shows the undeformed configuration and exaggerated displacement profile with the magnitude of the resulting displacement field superimposed. The von Mises stress profile is shown in Figure 26. Note that a logarithmic scale for the stress is used to more clearly visualize the changes in stress over the surface. A closeup of the von Mises stress solution near extraordinary points is shown in Figure 27. Notice the smoothness of the resulting stress profile.

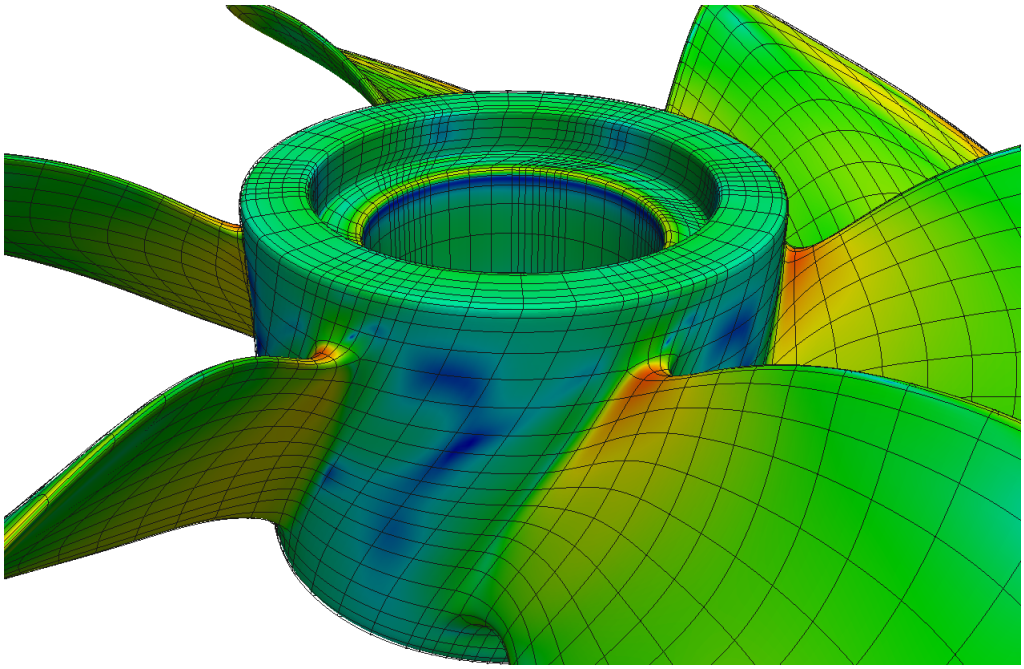

Figure 27: The von Mises stress solution near extraordinary points

11. Conclusion

We have extended the definition of analysis-suitable T-splines to encompass surfaces of arbitrary topological complexity. The smooth T-spline basis functions near extraordinary points are defined entirely in terms of polynomial Bézier elements thus standardizing the element representation for the entire surface. Additionally, we developed a collocation approach which properly accounts for T-junctions and extraordinary points.

We have developed an isogeometric collocated boundary element method using unstructured T-spline surfaces with particular emphasis on linear elastostatic problems. We have demonstrated the method on several three dimensional benchmark problems and shown the potential of the method to handle complex, real-world geometries in a fully automated manner, in the context of a T-spline propeller model. The T-spline CAD file was created by a designer. There was no alteration to it for the purposes of analysis, no feature removal, no geometry clean-up, no mesh generation. The results illustrate the power of the isogeometric vision. There is one and only one design/analysis model – the T-spline surface.

In this work we used high-order Gaussian quadrature rules on Bézier elements, but these are quite inefficient. In future work, we plan on developing adaptive quadrature schemes which properly account for nearly singular and singular integrals and which take advantage of the smoothness of the underlying T-spline basis [110]. We also plan on extending the range of applicability of the method to encompass other areas of application.

Acknowledgements

Robert Simpson and Stéphane Bordas would like to acknowledge the partial financial support of the Framework Programme 7 Initial Training Network Funding (289361) "Integrating Numerical Simulation and Geometric Design Technology" and the UK Engineering and Physical Science Research Council (EPSRC) (EP/G069352/1) "Advanced discretisation strategies for 'atomistic' nano CMOS simulation." Stéphane Bordas also thanks partial funding for his time provided by the EPSRC (EP/G042705/1) "Increased Reliability for Industrially Relevant Automatic Crack Growth Simulation with the eXtended Finite Element Method" and a European Research Council Starting Independent Research Grant (279578). Robert Simpson is grateful for funding received from the J.T. Oden Visitors Program which sponsored a visit to the Institute of Computational and Engineering Sciences, U.T. Austin in January 2012. M.A. Scott, J.A. Evans, S. Lipton, and T.J.R. Hughes were supported by grants from the Office of Naval Research (N00014-08-1-0992), the National Science Foundation (CMMI-01101007), and SINTEF (UTA10-000374), with the University of Texas at Austin. T. W. Sederberg was supported by a grant from the Office of Naval Research (N00014-08-C-0920).

Appendix A. A non-uniform T-spline to Bézier transformation

Referring to Figure 3b, the linear combinations defining the four face points are

$$\mathbf{Q}_6^f = \left(\frac{b+c}{a+b+c}\right)\left(\frac{e+f}{d+e+f}\right)\mathbf{P}_A + \left(\frac{b+c}{a+b+c}\right)\left(\frac{d}{d+e+f}\right)\mathbf{P}_B + \left(\frac{a}{a+b+c}\right)\left(\frac{d}{d+e+f}\right)\mathbf{P}_C + \left(\frac{a}{a+b+c}\right)\left(\frac{e+f}{d+e+f}\right)\mathbf{P}_D, \tag{A.1}$$

$$\mathbf{Q}_7^f = \left(\frac{b+c}{a+b+c}\right)\left(\frac{f}{d+e+f}\right)\mathbf{P}_A + \left(\frac{b+c}{a+b+c}\right)\left(\frac{d+e}{d+e+f}\right)\mathbf{P}_B + \left(\frac{a}{a+b+c}\right)\left(\frac{d+e}{d+e+f}\right)\mathbf{P}_C + \left(\frac{a}{a+b+c}\right)\left(\frac{f}{d+e+f}\right)\mathbf{P}_D, \tag{A.2}$$

$$\mathbf{Q}_{10}^f = \left(\frac{c}{a+b+c}\right)\left(\frac{e+f}{d+e+f}\right)\mathbf{P}_A + \left(\frac{c}{a+b+c}\right)\left(\frac{d}{d+e+f}\right)\mathbf{P}_B + \left(\frac{a+b}{a+b+c}\right)\left(\frac{d}{d+e+f}\right)\mathbf{P}_C + \left(\frac{a+b}{a+b+c}\right)\left(\frac{e+f}{d+e+f}\right)\mathbf{P}_D, \tag{A.3}$$

and

$$\mathbf{Q}_{11}^f = \left(\frac{c}{a+b+c}\right)\left(\frac{f}{d+e+f}\right)\mathbf{P}_A + \left(\frac{c}{a+b+c}\right)\left(\frac{d+e}{d+e+f}\right)\mathbf{P}_B + \left(\frac{a+b}{a+b+c}\right)\left(\frac{d+e}{d+e+f}\right)\mathbf{P}_C + \left(\frac{a+b}{a+b+c}\right)\left(\frac{f}{d+e+f}\right)\mathbf{P}_D, \tag{A.4}$$

where bold upper-case letters denote control points and lower case letters denote knot intervals.

Referring to Figure 3c, any two edge points along an edge are defined as

$$\mathbf{Q}_i^e = \left(\frac{a}{a+b}\right)\mathbf{Q}_a^f + \left(\frac{b}{a+b}\right)\mathbf{Q}_d^f \tag{A.5}$$

and

$$\mathbf{Q}_j^e = \left(\frac{a}{a+b}\right)\mathbf{Q}_b^f + \left(\frac{b}{a+b}\right)\mathbf{Q}_c^f. \tag{A.6}$$

Finally, referring to Figure 3d, each vertex point is defined as

$$\mathbf{Q}_j^v = \sum_{i=1}^{N}\left(\frac{a^{i-1}}{a^{i-1}+a^{i+1}}\right)\left(\frac{a^{i+2}}{a^i+a^{i+2}}\right)\mathbf{Q}_i^f. \tag{A.7}$$

Notice that both edge and vertex points are defined in terms of face points of neighboring Bézier elements. If the initial control mesh is a tensor product mesh these rules are equivalent to repeated knot insertion as presented in [53, 54].

Appendix B. Derivation of G^1 constrained minimization

We note that to assemble the global equation system for a one-ring neighborhood of irregular elements, the local indices for a Bézier coefficient, $c^{i,A}_{\alpha\beta}$, corresponding to the representation of N_A over the i^{th} irregular element must be mapped to a global index I. This map can be written as,

$$I(i,\alpha,\beta) = \begin{cases} \alpha,\beta = 1, & 1, \\ \alpha = 1, \beta \neq 1, & 20i+\beta \\ \alpha \neq 1, & 20(i-1)+4(\beta-1)+\alpha. \end{cases} \tag{B.1}$$

Figure B.28 shows the action of $I(i,\alpha,\beta)$ on the local indices of the Bézier coefficients, $c^{i,A}_{\alpha\beta}$.

Appendix B.1. Assembling the constraint equations

As a result of the T-spline to Bézier transformation, irregular element $\mathbf{w}^i$ is C^1-continuous with $\mathbf{x}^i$ and $\mathbf{z}^i$, $i = 1,\ldots,N$, as shown in Figure B.29. To maintain C^1 continuity between these elements during smoothing only requires that the Bézier coefficients remain the same. This is satisfied if the equations $\tilde{c}^A_{I(i,\alpha,\beta)} = c^{i,A}_{\alpha\beta}$ for $\alpha \geq 4$ and $\beta \geq 1$ or $2 \leq \alpha \leq 3$ and $\beta \geq 4$, $i = 1,\ldots,N$ are assembled into $\mathbf{G}_A$ and $\mathbf{g}_A$.

In addition to the C^1 constraints along the boundaries of the one-ring neighborhood we also enforce G^1 continuity along spoke edges. In other words, we must derive the constraint equations such that Bézier elements $\mathbf{w}^{i-1}$ and $\mathbf{w}^i$ are G^1-continuous for $i = 1,\ldots,N$. The general necessary and sufficient conditions for two Bézier elements to be G^1 is that they have the same normal vector along their common boundary curve. Bézier elements $\mathbf{w}^{i-1}$ and $\mathbf{w}^i$ in Figure B.29 are G^1 if there exists functions $a^i(\xi)$, $b^i(\xi)$, and $c^i(\xi)$ that satisfy

$$f^i(\xi) = a^i(\xi)\frac{\partial \mathbf{w}^{i-1}(\xi,\eta)}{\partial \eta}|_{\eta=0} + b^i(\xi)\frac{\partial \mathbf{w}^{i}(\xi,\eta)}{\partial \xi}|_{\eta=0} + c^i(\xi)\frac{\partial \mathbf{w}^{i}(\xi,\eta)}{\partial \eta}|_{\eta=0} \equiv 0 \tag{B.2}$$

$$= a^i(\xi)\mathbf{w}^{i-1}_\eta(\xi) + b^i(\xi)\mathbf{w}^i_\xi(\xi) + c^i(\xi)\mathbf{w}^i_\eta(\xi) \equiv 0. \tag{B.3}$$

We assign a shared local coordinate system for both elements where the local ξ parameter lies along their common boundary curve as shown in Figure B.29. Throughout, we adopt the notation

$$\langle c_1, c_2, \ldots, c_{p+1}\rangle^p(\xi) = \sum_{\alpha=1}^{p+1} c_\alpha B^p_\alpha(\xi) \tag{B.4}$$

where $B^p_\alpha(\xi)$ is a Bernstein polynomial of degree p in ξ. If $\mathbf{w}^{i-1}(\xi,\eta)$ and $\mathbf{w}^i(\xi,\eta)$ are biquartic then $a^i(\xi) = a^{i+1}$ and $c^i(\xi) = a^{i-1}$. In addition, $b^i(\xi)$ must be quadratic and the common boundary curve must be cubic. Then, the individual terms in (B.3) can be written as

$$a^i(\xi)\mathbf{w}^{i-1}_\eta(\xi) = 4a^{i+1}\langle c^{i-1}_{21} - c^i_{11}, c^{i-1}_{22} - c^i_{21}, c^{i-1}_{23} - c^i_{31}, c^{i-1}_{24} - c^i_{41}, c^{i-1}_{25} - c^i_{51}\rangle^4(\xi), \tag{B.5}$$

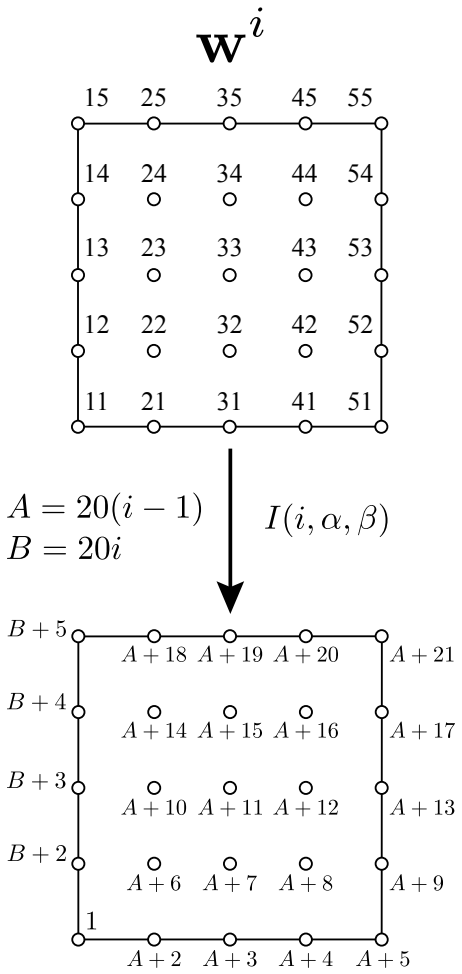

Figure B.28: The action of the local-to-global index map, $I(i, \alpha, \beta)$.

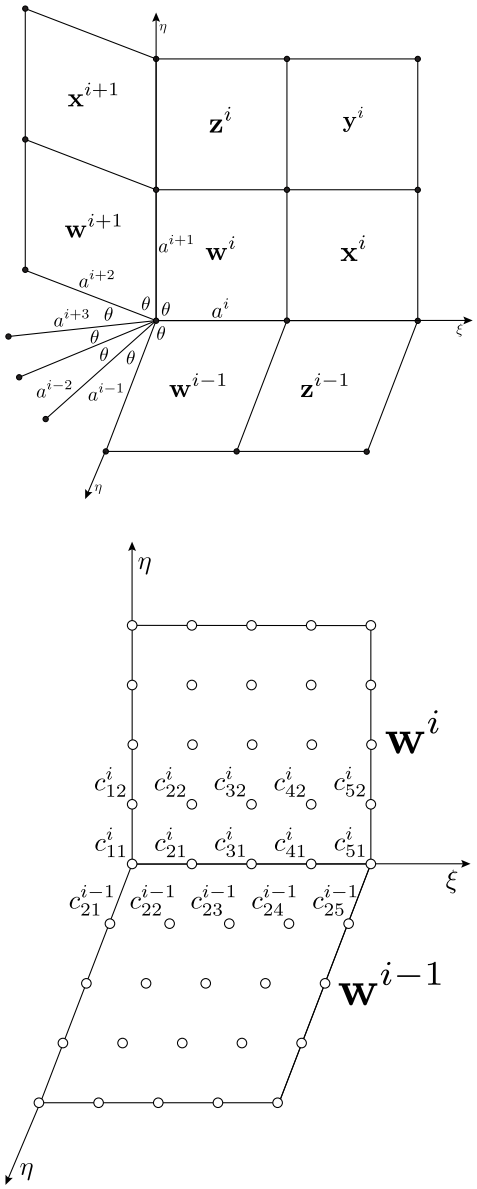

Figure B.29: The i^{th} quadrant of a two-ring neighborhood around an extraordinary point (top) and a close-up of the Bézier coefficients involved in the G^1 constraint equations (bottom). The $\mathbf{w}^i$, $\mathbf{x}^i$, $\mathbf{y}^i$, and $\mathbf{z}^i$ represent Bézier elements, the a^i represent knot intervals, and the $c^i_{\alpha\beta}$ denote Bézier coefficients used in the G^1 constraint equations (B.9) – (B.14).

$$b^i(\xi)\mathbf{w}^i_\xi(\xi) = \langle\lambda^i, 0, 0\rangle^2(\xi)\langle 4(c^i_{21} - c^i_{11}), 4(\frac{1}{4}c^i_{11} - c^i_{21} + c^i_{41} - \frac{1}{4}c^i_{51}), 4(c^i_{51} - c^1_{41})\rangle^2(\xi) \tag{B.6}$$

$$= \lambda^i\langle 4(c^i_{21} - c^i_{11}), (\frac{1}{2}c^i_{11} - 2c^i_{21} + 2c^i_{41} - \frac{1}{2}c^i_{51}), \frac{2}{3}(c^i_{51} - c^i_{41}), 0, 0\rangle^4(\xi), \tag{B.7}$$

and

$$c^i(\xi)\mathbf{w}^i_\eta(\xi) = 4a^{i-1}\langle c^i_{12} - c^i_{11}, c^i_{22} - c^i_{21}, c^i_{32} - c^i_{31}, c^i_{42} - c^i_{41}, c^i_{52} - c^i_{51}\rangle^4(\xi). \tag{B.8}$$

The equation $f^i(\xi)$ is a degree four polynomial in ξ which vanishes only if the following five terms vanish,

$$a^{i+1}(c^{i-1}_{21} - c^i_{11}) + \lambda^i(c^i_{21} - c^i_{11}) + a^{i-1}(c^i_{12} - c^i_{11}) = 0, \tag{B.9}$$

$$4a^{i+1}(c^{i-1}_{22} - c^i_{21}) + \lambda^i(\frac{1}{2}c^i_{11} - 2c^i_{21} + 2c^i_{41} - \frac{1}{2}a^i_{51}) + 4a^{i-1}(c^i_{22} - c^i_{21}) = 0, \tag{B.10}$$

$$4a^{i+1}(c^{i-1}_{23} - c^i_{31}) + \frac{2}{3}\lambda^i(c^i_{51} - c^i_{41}) + 4a^{i-1}(c^i_{32} - c^i_{31}) = 0, \tag{B.11}$$

$$a^{i+1}(c^{i-1}_{24} - c^i_{41}) + a^{i-1}(c^i_{42} - c^i_{41}) = 0, \tag{B.12}$$

$$a^{i+1}(c^{i-1}_{25} - c^i_{51}) + a^{i-1}(c^i_{52} - c^i_{51}) = 0. \tag{B.13}$$

To force the boundary curve to be a cubic polynomial requires that the fourth derivative vanishes. This constraint can be written as,

$$c^i_{11} - 4c^i_{21} + 6c^i_{31} - 4c^i_{41} + c^i_{51} = 0. \tag{B.14}$$

Notice that (B.9), (B.10), and (B.11) must be solved simultaneously for $i = 1, \ldots, N$. Equations (B.9), $i = 1, \ldots, N$, are often called *consistency conditions*. If we assume non-zero knot intervals, the solution for (B.9), $i = 1, \ldots, N$, requires that $c_{11}, c^1_{21}, \ldots, c^N_{21}$ all lie in a plane. Additionally, we impose the constraint that there exists an affine map that forces all angles marked θ in Figure B.28 to be equal and $|c^i_{21} - c^i_{11}|$ to be proportional to the knot intervals a^i_0. Under those restrictions, (B.9) is satisfied if

$$\lambda^i = -2\frac{a^{i-1}a^{i+1}}{a^i}\cos\theta \tag{B.15}$$

where $\theta = \frac{2\pi}{N}$.

The global constraint equations (B.9) – (B.14) are assembled into $\mathbf{G}_A$ and $\mathbf{g}_A$ for $i = 1, \ldots, N$ using the local-to-global map (B.1).

Appendix B.2. Assembling the fairing system

In contrast to more complicated fairing functionals commonly used in CAGD [92] we employ a very simple and efficient fairing technique which minimizes the vertical and horizontal differences between the Bézier coefficients resulting from the T-spline to Bézier transformation and the perturbed Bézier coefficients over each one-ring irregular element. In other words, the global equations

$$\tilde{c}^A_{I(i,\alpha,\beta)} - \tilde{c}^A_{I(i,\alpha+1,\beta)} = c^{i,A}_{\alpha\beta} - c^{i,A}_{\alpha+1\beta}, \quad 1 \leq \alpha \leq 4, 1 \leq \beta \leq 5 \tag{B.16}$$

and

$$\tilde{c}^A_{I(i,\alpha,\beta)} - \tilde{c}^A_{I(i,\alpha,\beta+1)} = c^{i,A}_{\alpha\beta} - c^{i,A}_{\alpha\beta+1}, \quad 1 \leq \alpha \leq 5, 1 \leq \beta \leq 4 \tag{B.17}$$

are assembled into $\mathbf{F}_A$ and $\mathbf{f}_A$ for $i = 1, \ldots, N$.

Appendix C. The challenge of discontinuous tractions

The challenge of robustly incorporating discontinuous tractions into a boundary element discretization scheme has been addressed by various authors. Unfortunately, there does not seem to be a general consensus on a preferred approach in the literature. The more prominent methods include:

1. Ignore the requirement that tractions be discontinous at corners and edges and assume that the errors are restricted to localized points on the boundary [103].
2. Force both displacements and tractions to be discontinuous at corners and edges [111].
3. Incorporate additional equations which relate tractions on either side of the edge into the system of equations [112].
4. Add collocation points where there are insufficient equations to solve for all traction unknowns [113].

We can immediately eliminate Method 2 since we view continuity of displacements as a fundamental physical constraint. We eliminate Method 3 because it introduces unnecessary implementational difficulties.

To decide between Method 1 and Method 4 a simple two-dimensional patch test is performed to compare their performance. Figure C.30 illustrates the problem of a square with Young's modulus E and Poisson's ratio ν under uniaxial tension. Exact displacements are specified at all points around the boundary while solving for tractions. The simple geometry is modeled using a cubic NURBS curve.

First applying the strategy outlined in Method 1, the collocation points are chosen to be equivalent to the classical Greville abscissae [63]. The resulting Bezier mesh is shown in Figure C.31a where, in this case, there is a single Bézier element per side. We model both displacements and tractions as continuous. The resulting traction profile is shown in Figure C.31b where it is clear that significant errors are introduced at corners. This in turn affects the accuracy of internal displacements since internal displacements depend on the boundary tractions. This behavior is greatly magnified in three-dimensional problems. For this reason, we eliminate Method 1 as a viable option.

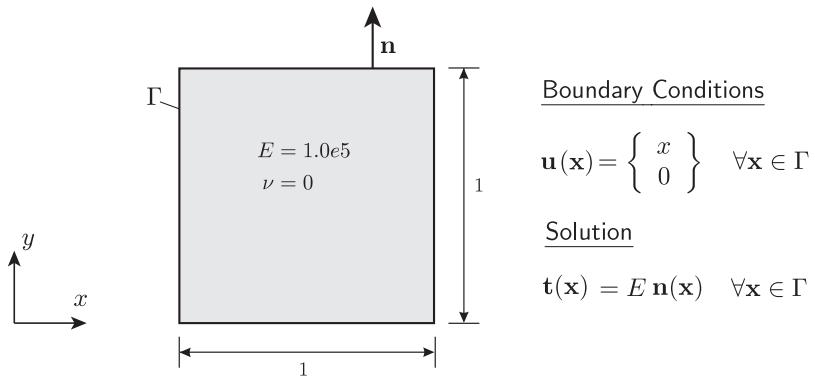

Figure C.30: A two-dimensional uniaxial tension problem

The remaining strategy (Method 4) is now tested. Since each corner exhibits unknown tractions on each side of the corner point, two collocation points are required at these locations. Each collocation point is offset by a small parameter into the interior of the element. An example mesh using this strategy is illustrated in Figure C.31c again using one Bézier element per side. Tractions are now allowed to be discontinuous at corner points, while displacements remain continuous as described in Section 7.1. The resulting traction profile in Figure C.31d illustrates the vast improvement over the previous approach. In addition, a mesh with two Bézier elements per side (Figure C.31c) shows that tractions can be both modeled as discontinuous at corners and continuous (C^2-continuous in this case) elsewhere while maintaing the accuracy of the solution (Figure C.31f).

An additional test is performed to ensure that the collocation strategy remains accurate under a nonlinear mapping from parametric space to physical space. This is achieved by modifying the knot vector used to construct the mesh in Figure C.31e such that the elements on the bottom and right faces of the mesh are unequal in length (see Figure C.31g) and exhibit nonlinear jacobians. The collocation strategy is insensitive to the nonlinear mapping resulting in accurately computed tractions .

Appendix D. Derivation of the jump term through rigid body motion

The jump term $\mathbf{C}$ in (1) can be related to the integral containing T_{ij} by applying rigid body motion. This is equivalent to the statement that

$$\mathbf{u}(\mathbf{x}) = \mathbf{1},\ \mathbf{t}(\mathbf{x}) = \mathbf{0} \quad \forall \mathbf{x} \in \Gamma. \tag{D.1}$$

Substituting this into (1) gives

$$\mathbf{C}(\mathbf{s}) + \int\!\!\!\!\!\!-_{\Gamma} \mathbf{T}(\mathbf{s}, \mathbf{x})\, \mathrm{d}\Gamma(\mathbf{x}) = 0 \tag{D.2}$$

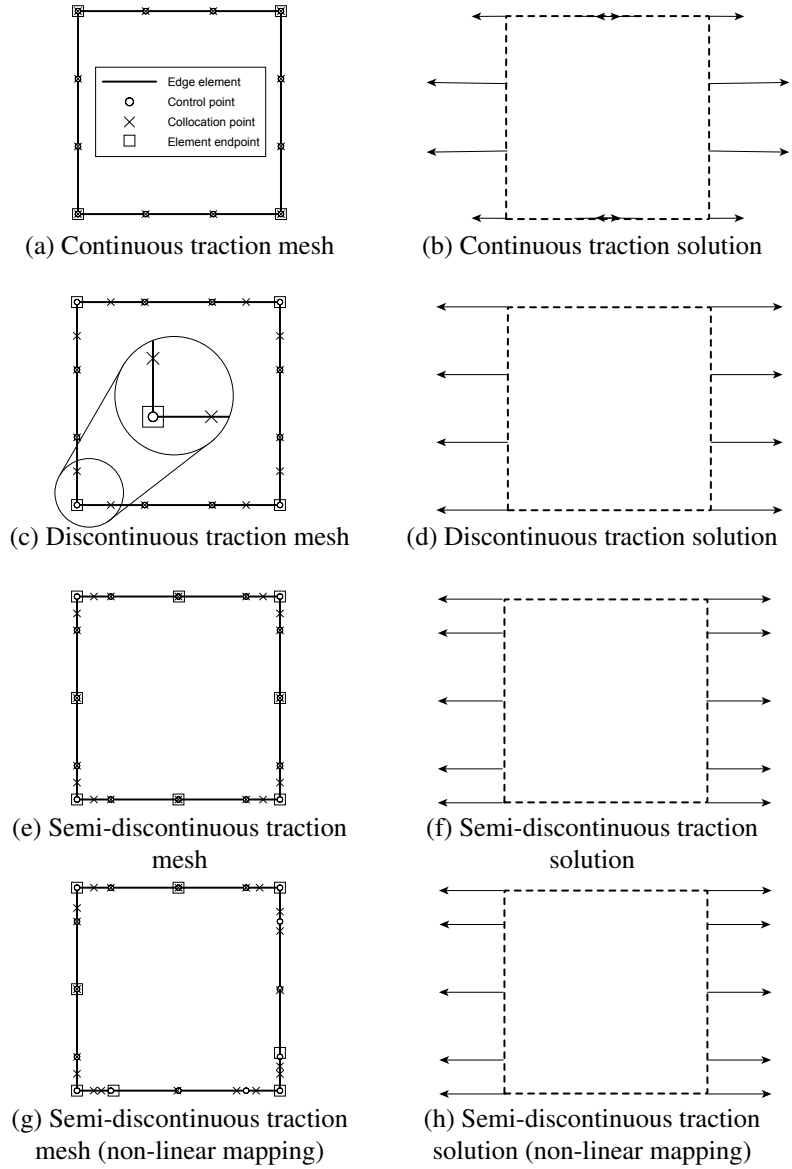

(a) Continuous traction mesh

(b) Continuous traction solution

(c) Discontinuous traction mesh

(d) Discontinuous traction solution

(e) Semi-discontinuous traction mesh

(f) Semi-discontinuous traction solution

(g) Semi-discontinuous traction mesh (non-linear mapping)

(h) Semi-discontinuous traction solution (non-linear mapping)

Figure C.31: A comparison of discretization and collocation strategies in the presence of discontinuous tractions. The configurations shown are all in physical space.

which implies that the jump term is

$$\mathbf{C}(\mathbf{s}) = -\cancel{\int}_{\Gamma} \mathbf{T}(\mathbf{s}, \mathbf{x})\, \mathrm{d}\Gamma(\mathbf{x}). \tag{D.3}$$

This relation circumvents the need to calculate $\mathbf{C}$ explicity (e.g. [114, 115]).

Appendix E. Expressions required for evaluation of boundary stresses

Displacement derivatives, in terms of the local coordinate system illustrated in Figure 8, can be derived using elementary geometric expression. We have that

$$v_1 = |\mathbf{m_1}|\xi + |\mathbf{m_2}|\eta\cos\theta \tag{E.1}$$

$$v_2 = |\mathbf{m_1}|\eta\sin\theta \tag{E.2}$$

where θ is the angle between m_1 and m_2 and is calculated from

$$\cos\theta = \frac{\mathbf{m_1}\cdot\mathbf{m_2}}{|\mathbf{m_1}||\mathbf{m_2}|}. \tag{E.3}$$

Rearranging (E.1) and substituting (E.2) for η, we have that

$$\xi = \frac{1}{|\mathbf{m_1}|}\left(v_1 - v_2\frac{\cos\theta}{\sin\theta}\right). \tag{E.4}$$

Similarly, (E.2) can be rewritten in terms of η as

$$\eta = \frac{v_2}{|\mathbf{m_2}|\sin\theta}. \tag{E.5}$$

From these expressions, the following derivatives can be found

$$\begin{aligned} \frac{\partial\xi}{\partial v_1} &= \frac{1}{|\mathbf{m_1}|}, \quad \frac{\partial\xi}{\partial v_2} = -\frac{1}{|\mathbf{m_1}|}\frac{\cos\theta}{\sin\theta} \\ \frac{\partial\eta}{\partial v_1} &= 0, \quad \frac{\partial\eta}{\partial v_2} = \frac{1}{|\mathbf{m_2}|\sin\theta}. \end{aligned} \tag{E.6}$$

Now, the displacement derivatives in the local coordinate system can be found. For example, $\partial u_1/\partial v_1$ can be written as

$$\frac{\partial u_1}{\partial v_1} = \begin{bmatrix} \frac{\partial u_x}{\partial\xi}\frac{\partial\xi}{\partial v_1} + \frac{\partial u_x}{\partial\eta}\frac{\partial\eta}{\partial v_1} \\ \frac{\partial u_y}{\partial\xi}\frac{\partial\xi}{\partial v_1} + \frac{\partial u_y}{\partial\eta}\frac{\partial\eta}{\partial v_1} \\ \frac{\partial u_z}{\partial\xi}\frac{\partial\xi}{\partial v_1} + \frac{\partial u_z}{\partial\eta}\frac{\partial\eta}{\partial v_1} \end{bmatrix} \cdot \begin{bmatrix} v_{1x} \\ v_{1y} \\ v_{1z} \end{bmatrix} \tag{E.7}$$

where (u_x, u_y, u_z) are the global displacement components and (v_{1x}, v_{1y}, v_{1z}) are the components of the vector $\mathbf{v_1}$. Similar expressions can be obtained for $\partial u_2/\partial v_2$, $\partial u_1/\partial v_2$ and $\partial u_2/\partial v_1$.

A transformation $\mathbf{R}$ between the local and global coordinate systems shown in Figure 8 is

$$\mathbf{R} = \begin{bmatrix} \mathbf{v_1}\cdot\mathbf{e}_1 & \mathbf{v_1}\cdot\mathbf{e}_2 & \mathbf{v_1}\cdot\mathbf{e}_3 \\ \mathbf{v_2}\cdot\mathbf{e}_1 & \mathbf{v_2}\cdot\mathbf{e}_2 & \mathbf{v_2}\cdot\mathbf{e}_3 \\ \mathbf{v_3}\cdot\mathbf{e}_1 & \mathbf{v_3}\cdot\mathbf{e}_2 & \mathbf{v_3}\cdot\mathbf{e_3} \end{bmatrix}. \tag{E.8}$$

[1] T. J. R. Hughes, J. A. Cottrell, Y. Bazilevs, Isogeometric analysis: CAD, finite elements, NURBS, exact geometry, and mesh refinement, Computer Methods in Applied Mechanics and Engineering 194 (2005) 4135–4195.

[2] J. A. Cottrell, T. J. R. Hughes, Y. Bazilevs, Isogeometric analysis: Toward Integration of CAD and FEA, Wiley, Chichester, 2009.

[3] J. A. Cottrell, A. Reali, Y. Bazilevs, T. J. R. Hughes, Isogeometric analysis of structural vibrations, Computer Methods in Applied Mechanics and Engineering 195 (2006) 5257–5296.

[4] J. A. Evans, Y. Bazilevs, I. Babuška, T. J. R. Hughes, n-widths, sup-infs, and optimality ratios for the k-version of the isogeometric finite element method, Computer Methods in Applied Mechanics and Engineering 198 (21-26) (2009) 1726–1741.

[5] I. Akkerman, Y. Bazilevs, V. Calo, T. J. R. Hughes, S. Hulshoff, The role of continuity in residual-based variational multiscale modeling of turbulence, Computational Mechanics 41 (2008) 371–378.

[6] Y. Bazilevs, V. M. Calo, J. A. Cottrell, T. J. R. Hughes, A. Reali, G. Scovazzi, Variational multiscale residual-based turbulence modeling for large eddy simulation of incompressible flows, Computer Methods in Applied Mechanics and Engineering 197 (2007) 173–201.

[7] Y. Bazilevs, I. Akkerman, Large eddy simulation of turbulent Taylor-Couette flow using isogeometric analysis and residual-based variational multiscale method, Journal of Computational Physics 229 (2010) 3402–3414.

[8] Y. Bazilevs, C. Michler, V. M. Calo, T. J. R. Hughes, Isogeometric variational multiscale modeling of wall-bounded turbulent flows with weakly enforced boundary conditions on unstretched meshes, Computer Methods in Applied Mechanics and Engineering 199 (13-16) (2010) 780–790.

[9] Y. Bazilevs, V. M. Calo, Y. Zhang, T. J. R. Hughes, Isogeometric fluid-structure interaction analysis with applications to arterial blood flow, Computational Mechanics 38 (2006) 310–322.

[10] Y. Bazilevs, V. M. Calo, T. J. R. Hughes, Y. Zhang, Isogeometric fluid-structure interaction: Theory, algorithms, and computations, Computational Mechanics 43 (2008) 3–37.

[11] Y. Zhang, Y. Bazilevs, S. Goswami, C. Bajaj, T. J. R. Hughes, Patient-specific vascular NURBS modeling for isogeometric analysis of blood flow, Computer Methods in Applied Mechanics and Engineering 196 (2007) 2943–2959.

[12] Y. Bazilevs, J. R. Gohean, T. J. R. Hughes, R. D. Moser, Y. Zhang, Patient-specific isogeometric fluid-structure interaction analysis of thoracic aortic blood flow due to implantation of the Jarvik 2000 left ventricular assist device, Computer Methods in Applied Mechanics and Engineering 198 (45-46) (2009) 3534–3550.

[13] F. Auricchio, L. B. da Veiga, C. Lovadina, A. Reali, The importance of the exact satisfaction of the incompressibility constraint in nonlinear elasticity: mixed FEMs versus NURBS-based approximations, Computer Methods in Applied Mechanics and Engineering 199 (2010) 314–323.

[14] F. Auricchio, L. B. da Veiga, A. Buffa, C. Lovadina, A. Reali, G. Sangalli, A fully "locking-free" isogeometric approach for plane linear elasticity problems: A stream function formulation, Computer Methods in Applied Mechanics and Engineering 197 (2007) 160–172.

[15] T. Elguedj, Y. Bazilevs, V. M. Calo, T. J. R. Hughes, $\bar{B}$ and $\bar{F}$ projection methods for nearly incompressible linear and non-linear elasticity and plasticity using higher-order NURBS elements, Computer Methods in Applied Mechanics and Engineering 197 (2008) 2732–2762.

[16] J. A. Cottrell, T. J. R. Hughes, A. Reali, Studies of refinement and continuity in isogeometric analysis, Computer Methods in Applied Mechanics and Engineering 196 (2007) 4160–4183.

[17] D. J. Benson, Y. Bazilevs, M. C. Hsu, T. J. R. Hughes, Isogeometric shell analysis: The Reissner-Mindlin shell, Computer Methods in Applied Mechanics and Engineering 199 (5-8) (2010) 276–289.

[18] D. J. Benson, Y. Bazilevs, M. C. Hsu, T. J. R. Hughes, A large deformation, rotation-free, isogeometric shell, International Journal for Numerical Methods in Engineering, 200 (2011) 1367 – 1378.

[19] D. J. Benson, Y. Bazilevs, E. De Luycker, M. C. Hsu, M. A. Scott, T. J. R. Hughes, T. Belytschko, A generalized finite element formulation for arbitrary basis functions: From isogeometric analysis to XFEM, International Journal for Numerical Methods in Engineering 83 (2010) 765–785.

[20] R. Echter, M. Bischoff, Numerical efficiency, locking and unlocking of NURBS finite elements, Computer Methods in Applied Mechanics and Engineering 199 (5-8) (2010) 374–382.

[21] J. Kiendl, Y. Bazilevs, M. C. Hsu, R. Wuechner, K. U. Bletzinger, The bending strip method for isogeometric analysis of Kirchhoff-Love shell structures comprised of multiple patches, Computer Methods in Applied Mechanics and Engineering 199 (37-40) (2010) 2403–2416.

[22] H. Gomez, V. M. Calo, Y. Bazilevs, T. J. R. Hughes, Isogeometric analysis of the Cahn-Hilliard phase-field model, Computer Methods in Applied Mechanics and Engineering 197 (2008) 4333–4352.

[23] H. Gomez, T. J. R. Hughes, X. Nogueira, V. M. Calo, Isogeometric analysis of the isothermal Navier-Stokes-Korteweg equations, Computer Methods in Applied Mechanics and Engineering 199 (25-28) (2010) 1828–1840.

[24] M. J. Borden, M. A. Scott, C. V. Verhoosel, C. M. Landis, T. J. R. Hughes, A phase-field description of dynamic brittle fracture, Computer Methods in Applied Mechanics and Engineering 217 (2012) 77 – 95.

[25] S. Lipton, J. A. Evans, Y. Bazilevs, T. Elguedj, T. J. R. Hughes, Robustness of isogeometric structural discretizations under severe mesh distortion, Computer Methods in Applied Mechanics and Engineering 199 (5-8) (2010) 357–373.

[26] W. A. Wall, M. A. Frenzel, C. Cyron, Isogeometric structural shape optimization, Computer Methods in Applied Mechanics and Engineering 197 (2008) 2976–2988.

[27] X. Qian, Full analytical sensitivities in NURBS based isogeometric shape optimization, Computer Methods in Applied Mechanics and Engineering 199 (29-32) (2010) 2059–2071.

[28] A. P. Nagy, M. M. Abdalla, Z. Gurdal, Isogeometric sizing and shape optimization of beam structures, Computer Methods in Applied Mechanics and Engineering 199 (17-20) (2010) 1216–1230.

[29] A. P. Nagy, M. M. Abdalla, Z. Gurdal, On the variational formulation of stress constraints in isogeometric design, Computer Methods in Applied Mechanics and Engineering 199 (41-44) (2010) 2687–2696.

[30] A. Buffa, G. Sangalli, R. Vázquez, Isogeometric analysis in electromagnetics: B-splines approximation, Computer Methods in Applied Mechanics and Engineering 199 (17-20) (2010) 1143–1152.

[31] E. Cohen, T. Martin, R. M. Kirby, T. Lyche, R. F. Riesenfeld, Analysis-aware modeling: Understanding quality considerations in modeling for isogeometric analysis, Computer Methods in Applied Mechanics and Engineering 199 (5-8) (2010) 334–356.

[32] J. Lu, Circular element: Isogeometric elements of smooth boundary, Computer Methods in Applied Mechanics and Engineering 198 (30-32) (2009) 2391–2402.

[33] H. Kim, Y. Seo, S. Youn, Isogeometric analysis for trimmed CAD surfaces, Computer Methods in Applied Mechanics and Engineering 198 (37-40) (2009) 2982–2995.

[34] P. Costantini, C. Manni, F. Pelosi, M. L. Sampoli, Quasi-interpolation in isogeometric analysis based on generalized B-splines, Computer Aided Geometric Design 27 (8) (2010) 656–668.

[35] M. Aigner, C. Heinrich, B. Juettler, E. Pilgerstorfer, B. Simeon, A. V. Vuong, Swept Volume Parameterization for Isogeometric Analysis, in: Hancock, E. R. and Martin, R. R. and Sabin, M. A. (Ed.), Mathematics of Surfaces XIII, Vol. 5654 of Lecture Notes in Computer Science, 2009, pp. 19–44.

[36] T. Martin, E. Cohen, R. M. Kirby, Volumetric parameterization and trivariate B-spline fitting using harmonic functions, Computer Aided Geometric Design 26 (6) (2009) 648–664.

[37] W. Wang, Y. Zhang, Wavelets-based NURBS simplification and fairing, Computer Methods in Applied Mechanics and Engineering 199 (5-8) (2010) 290–300. doi:10.1016/j.cma.2009.04.003.

[38] W. Wang, Y. Zhang, M. A. Scott, T. J. R. Hughes, Converting an unstructured quadrilateral mesh to a standard T-spline surface, Computational Mechanics, 48 (2011) 477 – 498.

[39] T. W. Sederberg, J. Zheng, A. Bakenov, A. Nasri, T-splines and T-NURCCs, ACM Trans. Graph. 22 (2003) 477–484.

[40] T. W. Sederberg, G. T. Finnigan, X. Li, H. Lin, Watertight trimmed NURBS, ACM Trans. Graph. 27 (2008) 1–79.

[41] H. Ipson, T-spline merging, Master's thesis, Brigham Young University (2005).

[42] T. W. Sederberg, D. L. Cardon, G. T. Finnigan, N. S. North, J. Zheng, T. Lyche, T-spline simplification and local refinement, ACM Trans. Graph. 23 (2004) 276–283.

[43] M. A. Scott, X. Li, T. W. Sederberg, T. J. R. Hughes, Local refinement of analysis-suitable T-splines, Computer Methods in Applied Mechanics and Engineering 213 (2012) 206 – 222.

[44] Y. Bazilevs, V. M. Calo, J. A. Cottrell, J. A. Evans, T. J. R. Hughes, S. Lipton, M. A. Scott, T. W. Sederberg, Isogeometric analysis using T-splines, Computer Methods in Applied Mechanics and Engineering 199 (5-8) (2010) 229–263.

[45] M. Dörfel, B. Jüttler, B. Simeon, Adaptive isogeometric analysis by local *h*-refinement with T-splines, Computer Methods in Applied Mechanics and Engineering 199 (5–8) (2009) 264–275.

[46] M. A. Scott, T-splines as a Design-Through-Analysis technology, Ph.D. thesis, The University of Texas at Austin (2011).

[47] X. Li, J. Zheng, T. W. Sederberg, T. J. R. Hughes, M. A. Scott, On linear independence of T-spline blending functions, Computer Aided Geometric Design 29 (2012) 63 – 76.

[48] C. V. Verhoosel, M. A. Scott, T. J. R. Hughes, de Borst, R., An isogeometric analysis approach to gradient damage models, International Journal for Numerical Methods in Engineering, 86 (2011) 115–134.

[49] C. V. Verhoosel, M. A. Scott, R. de Borst, T. J. R. Hughes, An isogeometric approach to cohesive zone modeling, International Journal for Numerical Methods in Engineering, 87 (2011) 336 – 360.

[50] Y. Bazilevs, M. C. Hsu, M. A. Scott, Isogeometric fluid-structure interaction analysis with emphasis on non-matching discretizations, and with application to wind turbines, Computer Methods in Applied Mechanics and Engineering submitted for publication.

[51] D. Schillinger, L. Dedé, M. A. Scott, J. A. Evans, M. J. Borden, E. Rank, T. J. R. Hughes, An isogeometric design-through-analysis methodology based on adaptive hierarchical refinement of NURBS, immersed boundary methods, and T-spline CAD surfaces, Computer Methods in Applied Mechanics and Engineering accepted for publication.

[52] Y. Zhang, W. Wang, T. J. R. Hughes, Solid T-spline construction from boundary representations for genus-zero geometry, ICES Report 11-40.

[53] M. J. Borden, M. A. Scott, J. A. Evans, T. J. R. Hughes, Isogeometric finite element data structures based on Bézier extraction of NURBS, International Journal for Numerical Methods in Engineering, 87 (2011) 15 – 47.

[54] M. A. Scott, M. J. Borden, C. V. Verhoosel, T. W. Sederberg, T. J. R. Hughes, Isogeometric Finite Element Data Structures based on Bézier Extraction of T-splines, International Journal for Numerical Methods in Engineering, 88 (2011) 126 – 156.

[55] L. Beirão da Veiga, A. Buffa, D. Cho, G. Sangalli, Isogeometric analysis using T-splines on two-patch geometries, Computer Methods in Applied Mechanics and Engineering 200 (21-22) (2011) 1787–1803.

[56] M. Jaswon, Integral equation methods in potential theory - i, Proc. Roy. Soc. Lond. A275 (1963) 23–32.

[57] G. Symm, Integral equation methods in potential theory - ii, Proc. Roy. Soc. Lond. A275 (1963) 33–46.

[58] T. Cruse, Numerical solutions in three dimensional elastostatics, International Journal of Solids and Structures 5 (1969) 1259–1274.

[59] J. Lachat, J. Watson, Effective numerical treatment of boundary integral equations: a formulation for three dimensional elastostatics, International Journal for Numerical Methods in Engineering 10 (1976) 991–1005.

[60] E. Cervera, J. Trevelyan, Evolutionary structural optimisation based on boundary representation of NURBS: Part I: 2D algorithms, Computers and Structures 23-24 (83) (2005) 1902–1916.

[61] E. Cervera, J. Trevelyan, Evolutionary structural optimisation based on boundary representation of NURBS: Part II: 3D algorithms, Computers and Structures 23-24 (83) (2005) 1917–1929.

[62] C. Politis, A. I. Ginnis, P. D. Kaklis, K. Belibassakis, C. Feurer, An isogeometric BEM for exterior potential-flow problems in the plane, in: 2009 SIAM/ACM Joint Conference on Geometric and Physical Modeling, SPM '09, 2009, pp. 349–354.

[63] R. Simpson, S. Bordas, J. Trevelyan, T. Rabczuk, A two-dimensional isogeometric boundary element method for elastostatic analysis, Computer Methods in Applied Mechanics and Engineering 209-212 (2012) 87–100.

[64] K. Li, X. Qian, Isogeometric analysis and shape optimization via boundary integral, Computer Aided Design 43 (11) (2011) 1427–1437.

[65] D. Arnold, W. L. Wendland, On the asymptotic convergence of collocation methods, Mathematics of Computation 41 (164) (1983) 349–381.

[66] J. Saranen, W. L. Wendland, On the asymptotic convergence of collocation methods with spline functions of even degree, Mathematics of Computation 45 (171) (1985) 91–108.

[67] G. Hsiao, S. Prössdorf, A generalization of the Arnold-Wendland lemma to a modified collocation method for boundary integral equations in $\mathbb{R}^3$, Mathematische Nachrichten 163 (1993) 133–144.

[68] M. Costabel, W. McLean, Spline collocation for strongly elliptic equations on the torus, Numer. Math. 62 (4) (1992) 511–538.

[69] P. Juhl, A note on the convergence of the direct collocation boundary element method, Journal of Sound and Vibration 212 (4) (1998) 703–719.

[70] T. J. R. Hughes, The Finite Element Method: Linear Static and Dynamic Finite Element Analysis, Dover Publications, Mineola, NY, 2000.

[71] A. Buffa, D. Cho, G. Sangalli, Linear independence of the T-spline blending functions associated with some particular T-meshes, Computer Methods in Applied Mechanics and Engineering 199 (23-24) (2010) 1437–1445.

[72] T. W. Sederberg, J. Zheng, X. Song, Knot intervals and multi-degree splines, Computer Aided Geometric Design 20 (2003) 455–468.

[73] E. Catmull, J. Clark, Recursively generated B-spline surfaces on arbitrary topological meshes, Computer Aided Design 10 (1978) 350–355.

[74] D. Doo, M. Sabin, Behaviour of recursive division surfaces near extraordinary points, Computer-Aided Design 10 (6) (1978) 356–360.

[75] C. Loop, Smooth subdivision surfaces based on triangles, Master's thesis, University of Utah (1987).

[76] M. Sabin, Recent progress in subdivision: A survey, Advances in Multiresolution for Geometric Modelling (2005) 203–230.

[77] U. Reif, A unified approach to subdivision algorithms near extraordinary vertices, Computer Aided Geometric Design 12 (2) (1995) 153–174.

[78] U. Reif, P. Schröder, Curvature integrability of subdivision surfaces, Advances in Computational Mathematics 14 (2) (2001) 157–174.

[79] J. Stam, Exact evaluation of Catmull-Clark subdivision surfaces at arbitrary parameter values, in: Proceedings of the 25th annual conference on Computer graphics and interactive techniques, ACM, 1998, pp. 395–404.

[80] T. J. Cashman, U. H. Augsdörfer, N. A. Dodgson, M. A. Sabin, NURBS with extraordinary points: high-degree, non-uniform, rational subdivision schemes, ACM Trans. Graph. 28 (2009) 46:1–46:9.

[81] T. W. Sederberg, J. Zheng, D. Sewell, M. Sabin, Non-uniform recursive subdivision surfaces, in: Proceedings of the 25th annual conference on Computer graphics and interactive techniques, SIGGRAPH '98, 1998, pp. 387–394.

[82] F. Cirak, M. Ortiz, P. Schröder, Subdivision surfaces: A new paradigm for thin shell analysis, International Journal for Numerical Methods in Engineering 47 (2000) 2039–2072.

[83] F. Cirak, M. Ortiz, Fully C^1-conforming subdivision elements for finite deformation thin shell analysis, International Journal for Numerical Methods in Engineering 51 (2001) 813–833.

[84] F. Cirak, M. J. Scott, E. K. Antonsson, M. Ortiz, P. Schröder, Integrated modeling, finite-element analysis, and engineering design for thin-shell structures using subdivision, Computer-Aided Design 34 (2002) 137–148.

[85] F. Cirak, M. Ortiz, A. Pandolfi, A cohesive approach to thin-shell fracture and fragmentation, Computer Methods in Applied Mechanics and Engineering 194 (21-24) (2005) 2604–2618.

[86] D. Burkhart, B. Hamann, G. Umlauf, Isogeometric finite element analysis based on Catmull-Clark subdivision solids, in: Computer Graphics Forum, Vol. 29, Wiley Online Library, 2010, pp. 1575–1584.

[87] W. Boehm, Visual continuity, Computer-Aided Design 20 (6) (1988) 307–311.

[88] W. L. F. Degen, Explicit continuity conditions for adjacent Bézier surface patches, Computer Aided Geometric Design 7 (1-4) (1990) 181–189.

[89] D. Liu, GC^1 continuity conditions between two adjacent rational Bézier surface patches, Computer Aided Geometric Design 7 (1-4) (1990) 151–163.

[90] J. Zheng, G. Wang, Y. Liang, Curvature continuity between adjacent rational Bézier patches, Computer Aided Geometric Design 9 (5) (1992) 321–335.

[91] J. Peters, Patching Catmull-Clark meshes, in: Proceedings of the 27th annual conference on computer graphics and interactive techniques, ACM Press/Addison-Wesley Publishing Co., 2000, pp. 255–258.

[92] C. Loop, S. Schaefer, G^2 tensor product splines over extraordinary vertices, in: Computer Graphics Forum, Vol. 27, Blackwell Science Ltd., 2008, pp. 1373–1382.

[93] X. Shi, T. Wang, P. Wu, F. Liu, Reconstruction of convergent G^1 smooth B-spline surfaces, Computer Aided Geometric Design 21 (9) (2004) 893–913.

[94] C. Loop, Second order smoothness over extraordinary vertices, in: Proceedings of the 2004 Eurographics/ACM SIGGRAPH symposium on Geometry processing, ACM, 2004, pp. 165–174.

[95] C. Loop, S. Schaefer, Approximating Catmull-Clark subdivision surfaces with bicubic patches, ACM Trans. Graph. 27 (2008) 1–11.

[96] Å. Björck, Numerical methods for least squares problems, Society for Industrial Mathematics, 1996.

[97] F. Auricchio, L. B. Da Veiga, T. J. R. Hughes, A. Reali, G. Sangalli, Isogeometric collocation methods, Mathematical Models and Methods in Applied Sciences 20 (11) (2010) 2075–2107.

[98] F. Auricchio, L. Beirao de Veiga, T. J. R. Hughes, A. Reali, G. Sangalli, Isogeometric collocation for elastostatics and explicit dynamics, ICES Report 12-07.

[99] J. Telles, A self-adaptive co-ordinate transformation for efficient numerical evaluation of general boundary element integrals, International Journal for Numerical Methods in Engineering 24 (5) (1987) 959–973.

[100] P. Johnston, D. Elliott, A sinh transformation for evaluating nearly singular boundary element integrals, International Journal for Numerical Methods in Engineering 62 (4) (2005) 564–578.

[101] Q. Huang, T. Cruse, Some notes on singular integral techniques in boundary element analysis, International Journal for Numerical Methods in Engineering 36 (15) (1993) 2643–2659.

[102] T. Cruse, R. Aithal, Non-singular boundary integral equation implementation, International Journal for Numerical Methods in Engineering 36 (2) (1993) 237–254.

[103] T. Cruse, An improved boundary-integral equation method for three dimensional elastic stress analysis, Computers and Structures 4 (1974) 741–754.

[104] Y. Liu, On the simple-solution method and non-singular nature of the BIE/BEM – a review and some new results, Engineering Analysis with Boundary Elements 24 (2000) 789–795.

[105] A. Becker, The Boundary Element Method in Engineering, McGraw-Hill Book Company, 1992.

[106] M. Aliabadi, The Boundary Element Method: Applications in Solids and Structures, John Wiley & Sons, 2002.

[107] T-Splines, Inc., http://www.tsplines.com/rhino/ (2011).

[108] G. P. Bazeley, Y. K. Cheung, B. M. Irons, O. C. Zienkiewicz, Triangular elements in plate bending—conforming and nonconforming solutions, in: Proceedings of the 1st Conference on Matrix Methods in Structural Mechanics, 1966, pp. 547–576.

[109] T. Takacs, B. Jüttler, Existence of stiffness matrix integrals for singularly parameterized domains in isogeometric analysis, Computer Methods in Applied Mechanics and Engineering 200 (2011) 3568–3582.

[110] T. J. R. Hughes, A. Reali, G. Sangalli, Efficient quadrature for NURBS-based isogeometric analysis, Computer Methods in Applied Mechanics and Engineering 199 (5-8) (2010) 301–313.

[111] Y. Mi, M. Aliabadi, Dual boundary element method for three-dimensional fracture mechanics analysis, Engineering Analysis with Boundary Elements 10 (2) (1992) 161–171.

[112] R. Rigby, M. Aliabadi, Out-of-core solver for large, multi-zone boundary element matrices, International Journal for Numerical Methods in Engineering 38 (1507–1533).

[113] S. Subia, M. Ingber, A. Mitra, A comparison of the semidiscontinuous element and multiple node with auxiliary boundary collocation approaches for the boundary element method, Engineering Analysis with Boundary Elements 15 (1) (1995) 19–27.

[114] V. Mantic, A new formula for the C-matrix in the Somigliana identity, Journal of Elasticity 33 (3) (1993) 191–201.

[115] F. Hartmann, The Somigliana identity on piecewise smooth surfaces, Journal of Elasticity 11 (4) (1981) 403–423.